Master in Nuclear Physics

Master Thesis

Nuclear quasi-bound states of antikaons and η mesons

Author:
Ignacio López de Arbina de Frutos

Advisor:
Prof. Àngels Ramos Gómez

Universitat de Barcelona

Dep. Física Quàntica i Astrofísica
Facultat de Física
Universitat de Barcelona

December 10, 2018

Acknowledgements

I would like to express my sincere gratitude to my advisor Prof. Àngels Ramos for her help and kind guidance along this work. Further, I would like to thank Prof. Mario Centelles for his help at a given point of the work when I felt stuck with the numerical procedure for solving the equations of the present thesis. Finally, I would like to thank my colleagues for their valuable comments and my family for their unconditional support.

In memory of my father.

Contents

Abstract

In this work we present a study on the mesic nuclear quasi-bound states, particularly on those of the $\bar{K}$ and η mesons. These states are formed when low energetic mesons bind to the nucleus for a short period of time due to the strong interaction.

In this scenario we test different theoretical meson-nucleus optical potentials by computing the binging energies and widths of the nuclear states. For the antikaons we employ in-medium amplitudes for a particular model while for the η meson we test five different models in the free-space, and one of them also in the nuclear medium.

Our results show an agreement with similar previous calculations, obtaining larger widths than the binding energies for the $\bar{K}$ nuclear quasi-bound states and smaller widths than the binding energies in the case of η nuclear quasi-bound states for two of the models studied.

Further, we devote a whole chapter to describe the numerical methods used to solve the Klein-Gordon equation describing the problem of the nuclear bound states, which constitutes the major part of this work. We explain step by step the main features of our code and the important considerations to take into account in order to obtain correct results.

Chapter 1

Introduction

Nothing great in the world was accomplished without passion.

— G. W. Hegel

1.1 Motivation

The study of exotic matter has been the target of many researches from the early fifties. The first studies date back to late forties, when Fermi and Teller [1] and Wheeler [2] postulated the existence of exotic atoms to explain the experimental results of Conversi [3], who observed the capture of negative muons by the nucleus. It is thought [4] that the first detection of negative pions was done by Camac [5] when studying the stopping of these particles in carbon.

Exotic atoms are atomic systems where heavy particles can replace an electron. Such particles have negative charge and need to have long enough lifetimes to form bound states with the nucleus before decay. For that reason, some of the particles of interest for hadronic atoms are π^-, K^-, Σ^- and $\bar{p}$. Due to the larger mass of these hadrons with respect to the electrons, the orbits that they occupy are much closer to the nucleus that the ones of the electrons. Besides, since only one hadron is captured by the nucleus, the Pauli principle does not apply, leaving the whole set of atomic levels free for the hadron. Thus, as a first approximation, one can focus in the hadron-nucleus system neglecting the presence of the electrons, what simplifies the study to that of the hydrogen-like atoms. However, hadrons interact strongly with the nucleus at low energies, bringing about information on the strong interaction, the matter distribution of the nucleus, precise values of the hadron masses and the magnetic moments [4].

The hadronic atom is formed when, in a nuclear reaction, a negatively charged hadron is stopped in the target and captured by the atoms that compose it. The captured hadron will cascade down through its atomic levels until arrive to a state with small principal quantum number where it will by absorbed by the nucleus due to the strong interaction. While falling towards the nucleus, it emits Auger electron and, in the last stages, its characteristics X-rays.

Since these hadrons have longer lifetimes than typical atomic scales well-defined atomic states can be formed, and the effects of the strong interaction can be studied. Further, due to the fact that the hadrons are much closer to the nucleus than the electrons, the tail of its atomic wave functions lies within the nuclear medium, hence providing information about the density dependence of the strong interaction [6].

However, the lower levels of the hadronic atoms can penetrate enough the nucleus such that the strong interaction with the nucleus produces wider level widths than those of the purely electromagnetic level. In this scenario, the emitted X-rays are highly suppressed in comparison with the nucleus absorption, hampering its detection by standard techniques as X-ray spectroscopy.

As it is shown in this work, the study of the strong interaction through hadron atomic levels is limited by the capacity of resolving these states with such large widths. Therefore, in order to obtain more information about the strong interaction one can study exotic nuclear states.

Exotic nuclei are nuclear systems that contain an additional exotic particle to the usual nucleons within the nucleus. In contrast to the exotic atomic levels, exotic nuclear states are produced when the strong interaction between the exotic particles and the nucleus is dominant with respect the electromagnetic interaction. Actually, non-charged particles are of great interest in these studies since they only interact strongly with the nucleus.

The experiments studying hadronic nuclear states have used different types of beams such as photons, pions, protons and light and heavy ions, with energies ranging from low to ultra-relativistic energies. Nonetheless, the energies of interest to study nuclear bound states are of the order of the production threshold or slightly above. This is because only slow enough hadrons would be captured by the nucleus, as long as there is sufficient attraction.

The study of mesic nuclear bound states is a suitable way of obtaining information on the strong interaction and serves as an appropriate testing scenario to understand the Quantum Chromodynamics theory (QCD) in the non-perturbative regime, as it is explained in the next section. The QCD theory contemplates mesons as excitations of its vacuum due to quark condensates, which are expected to change in the strongly interacting nuclear medium, thus modifying the mass spectrum of the mesons.

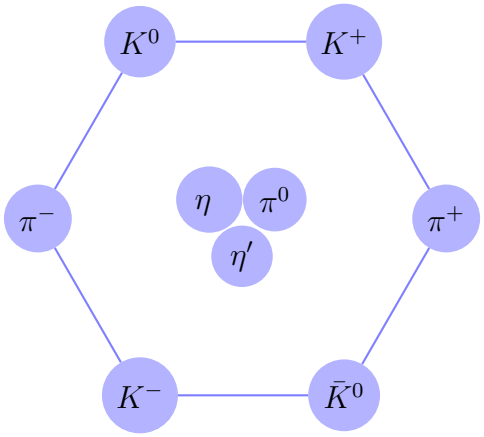

Figure 1.1. Representation of the pseudoscalar meson nonet of SU(3) group.

In this work we concentrate in the $S = -1$ sector of the pseudoscalar nonet of mesons, see Fig. 1.1, namely the antikaons $\bar{K} = (K^-, \bar{K}^0)$, as well as in the η meson. These particles are of interest due to the resonances that arise in their meson-nucleon interactions. In the case of the antikaons the $\Lambda(1405)$ resonance is produced below the $\bar{K}N$ threshold

Meson	V_0 (MeV)	W_0 (MeV)	σ_{unel} (mb)	Reaction	Collaboration	Ref.
K^+	$\simeq 25$	–	–	$p + A$	KaoS	[8]
K^+	15–20	–	–	Ru+Ru, Ni+Ni	FOPI	[9]
K^+	20 ± 3	–	–	$p + A$	ANKE	[10]
K^+	$\simeq 30$	–	–	Ni+Ni	–	[11]
K^+	20 ± 5	–	–	Ni+Ni	FOPI	[12]
K^0	20 ± 5	–	–	$\pi^- + A$	FOPI	[13]
K^0	$\simeq 49$	–	–	Ar + KCl	HADES	[14]
K^0	40 ± 5	–	–	p + Nb	HADES	[15]
K^-	$\simeq -80$	–	–	$p + A$	KaoS	[8]
K^-	$-(45 - 50)$	–	–	Ni+Ni	FOPI	[12]
K^-	-60^{+50}_{-31}	–	–	$p + A$	ANKE	[16]
K^-	$-160... - 190$	$\simeq -60$	–	^{12}C, ^{16}O(K^-, N)	KEK E548	[17]
η		$-$(10–30)	30 ± 6	$\gamma + A$	A2	[18]
η	$-(54 \pm 6)$	$-(20 \pm 2)$	–	$p + d$	ANKE, COSY11	[19]
η'	–	$-(10 \pm 2.5)$	10.3 ± 1.4	$\gamma + A$	CBELSA/TAPS	[20]
η'	–	$-(13 \pm 3 \pm 3)^*$	13 ± 3	γ + C, Nb	CBELSA/TAPS	[21]
η'	$-(37 \pm 10 \pm 10)$	–	–	γ + C	CBELSA/TAPS	[22]
η'	$-(41 \pm 10 \pm 15)$	–	–	γ + Nb	CBELSA/TAPS	[23]
ω	–	$-$(35–50)	$\simeq 40$	$\gamma + A$	CBELSA/TAPS	[24]
ω	–	$-(48 \pm 12 \pm 9)$	–	γ + C, Nb	CBELSA/TAPS	[21]
ω	$-(29 \pm 19 \pm 20)$	–	–	γ + C, Nb	A2	[25]
ω	$-(15 \pm 35 \pm 20)$	–	–	γ + C	CBELSA/TAPS	[26]
ω	$\simeq -75$	0	–	$p + A$	KEK E325	[27]
ω	–	≤ -100	–	$\gamma + A$	CLAS	[31]
ϕ	–	$-$(20–30)	–	$p + A$	ANKE	[29]
ϕ	–	$-$(10–30)	14–25	$p + A$	ANKE	[30]
ϕ	–	$-$(23–100)	16–70	$\gamma + A$	CLAS	[31]
ϕ	–	–	35^{+17}_{-11}	$\gamma + A$	LEPS	[32]
ϕ	$\simeq -35$	-7.5	–	$p + A$	KEK E325	[33]

Table 1.1. Experimentally deduced real (V_0) and imaginary (W_0) meson-nucleon potentials at normal nuclear matter density. The asterisk on the potential values stands for the extrapolated values to meson momentum zero, otherwise the values have been determined as an average over a momentum range, mainly $0 \ll p \leq m$. When giving separately in the original literature the first error refers to the statistical error and the second to the systematic error. (Table from Ref. [7])

—around 30 MeV below the $\bar{K}$ production threshold— and into $\pi\Sigma$. On the other hand, the ηN interaction is dominated by the $N^*(1535)$ baryon resonance which is located around 50 MeV above the production threshold.

The interest of the search for mesic nuclear states can be found in both nuclear and hadronic physics. In the case of nuclear physics these states are exotic configurations of nuclei since they correspond to states with excitation energies of several hundred MeV up to GeV. On the other hand, for hadron physics these states provide essential information to investigate meson properties and their modification at finite nuclear densities [7]. Considering an optical potential governing the meson-nucleon interaction, i.e.

$$V_{\text{opt}}(r) = V(r) + \mathrm{i}W(r), \tag{1.1}$$

the detection of mesic nuclear quasi-bound states will be enhanced if the depth

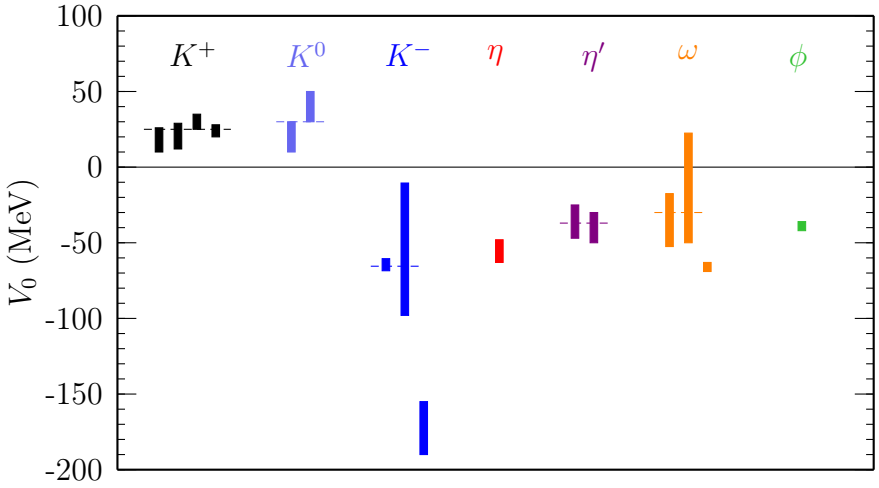

Figure 1.2. Graphical representation of the experimental data for the real part of the meson-nucleus potential depths of Table 1.1 for the K^+, K^0, K^-, η, η', ω and ϕ mesons.

of the real part of the optical potential is larger than the imaginary part of the optical potential, that is

$$|V| \gg |W|, \tag{1.2}$$

and if the energy of the quasi-bound state is larger than the energy width of the state.

The typical experimental procedures for the search of nuclear bound states is to look for structures similar to the resonances in the excitation energy range of the residual nucleus, where the meson-nucleus configuration is expected to take place. Then, the states can be detected by studying the meson decay or by missing-mass spectrometry. Another common procedure is to measure the production of the meson near the production threshold [7].

In Table 1.1 we present a compilation of the available experimental data of the meson-nucleon interaction. For completeness we also show the data for K^+, η', ω and ϕ mesons, although they are not discussed in this work. Figure 1.2 shows the plot of experimental the real part of the optical potential for the K^+, K^0, K^-, η, η', ω and ϕ mesons. The first thing one notices is that the K^+ and K^0 potential depths show a repulsive behaviour while for the other mesons this depth is attractive, although with different strength for the different mesons.

In the case of the antikaon, K^-, the experimental data for the strength of the real part of the potential lie in a wide range of values, from a minimum around -190 MeV to a maximum of about -20 MeV, including the uncertainties, while for the η meson the range is smaller and the value is around -50 MeV.

Figure 1.3 plots the experimental data for the imaginary part of the meson-nucleus optical potential for the K^-, η, η', ω and ϕ mesons. All of them are negative, what highlights the meson absorption in the nuclear medium.

The important feature for the formation of the meson nuclear quasi-bound states is the relative strength of the real and imaginary part of the optical potential as expressed in Eq. (1.2). In the case of the K^-, the widths are larger

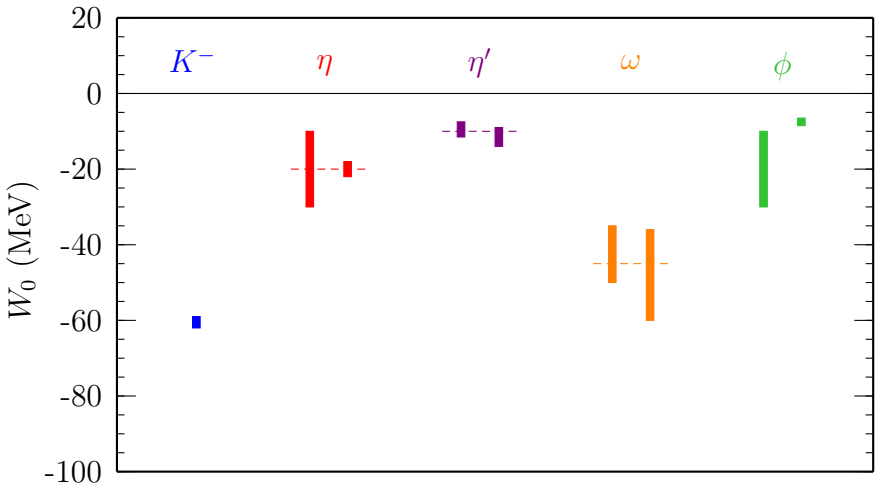

Figure 1.3. Graphical representation of the experimental data for the imaginary part of the meson-nucleus potential depths of Table 1.1 for the K^-, η, η', ω and ϕ mesons.

than the depths, which indicates that the absorption of the meson by the nucleus is more probable that the formation of a quasi-bound state. On the other hand, the experimental data for the η-nucleus optical potential seem to fulfil Eq. (1.2) enhancing the observation of η nuclear bound states.

1.2 Chiral effective meson-baryon interaction

The strong interaction is the force that governs the interaction between the fundamental constituents of the hadrons. It is explained by the quantum chromodynamics (QCD) theory, which is a SU(3) gauge theory where the fundamental fields are the quarks and the gauge fields are the gluons. The quark fields are formed by the three lightest quarks —u, d and s— which are treated as massless particles in this theory. In this framework, the lowest order QCD Lagrangian can be written as

$$\begin{aligned}\mathcal{L}^0_{\rm QCD} = &-\frac{1}{2}\,\mathrm{tr}[(\partial_\mu A_\nu - \partial_\nu A_\mu - \mathrm{i}g\,[A_\mu, A_\nu])\,(\partial^\nu A^\mu - \partial^\mu A^\nu - \mathrm{i}g\,[A^\mu, A^\nu])] \\ &+ \bar{q}\mathrm{i}\gamma^\mu\,(\partial_\mu - \mathrm{i}gA_\mu)\,q,\end{aligned} \tag{1.3}$$

where q represents the quark field and

$$A_\mu = \sum_a T^a A^a_\mu, \tag{1.4}$$

where A^a_μ are the gluon fields for $a = 1, \ldots, 8$ and $T^a = \lambda^a/2$ are the generators of the colour group SU(3) with λ^a Gell-Mann matrices, and g is the gluon gauge coupling constant.

The projection operators, $P_{\rm L,R} = (1 \mp \gamma_5)/2$, can be applied over the quark fields to define chiral eigenstates $q_{\rm L} = P_{\rm L} q$ and $q_{\rm R} = P_{\rm R} q$, for massless particles.

Since the projection operators fulfil completeness, $P_{\rm L}+P_{\rm R}=\mathbb{I}$, are idempotent, $P_{\rm L}^2=P_{\rm L}$ and $P_{\rm R}^2=P_{\rm R}$, and orthonormal, $P_{\rm L}P_{\rm R}=P_{\rm R}P_{\rm L}=0$, one can rewrite the lowest order QCD Lagrangian of Eq. (1.3) as

$$\begin{aligned}\mathcal{L}^0_{\rm QCD} = &-\frac{1}{2}\,{\rm tr}[(\partial_\mu A_\nu-\partial_\nu A_\mu-{\rm i}g\,[A_\mu,A_\nu])\,(\partial^\nu A^\mu-\partial^\mu A^\nu-{\rm i}g\,[A^\mu,A^\nu])]\\ &+\bar{q}_{\rm L}{\rm i}\gamma^\mu\,(\partial_\mu-{\rm i}gA_\mu)\,q_{\rm L}+\bar{q}_{\rm R}{\rm i}\gamma^\mu\,(\partial_\mu-{\rm i}gA_\mu)\,q_{\rm R}.\end{aligned}\tag{1.5}$$

This expression shows that $q_{\rm L}$ and $q_{\rm R}$ define two independent terms of the lowest order QCD Lagrangian. This property defines a global ${\rm SU_L}(3)\times{\rm SU_R}(3)$ symmetry, also know as chiral symmetry of QCD.

However, the expectation value of the $\bar{q}q$ operator over the vacuum, $\langle 0\,|\bar{q}q|\,0\rangle$, is nonzero. This creates a finite quark condensate that breaks the chiral symmetry spontaneously. By Nambu-Goldstone theorem [34, 35, 36] bosonic massless particles appear for each broken symmetry. In three-flavour (uds) QCD the lightest pseudoscalar mesons arise, that is π, K and η mesons.

To approach a more realistic description, nonzero masses should be added to the fermionic fields, q. By imposing this condition the chiral symmetry is broken explicitly generating masses for the Nambu-Golstone (NG) bosons.

Some of the the $\bar{K}N$ amplitudes used for the calculations in this work [37] have been computed using a chiral non-perturbative scheme, including the whole set of 0^- pseudoscalar mesons and the octet of $1/2^+$ baryons. The lowest order chiral Lagrangian that couples the octet of $1/2^+$ baryons and the octet of pseudoscalar mesons is given by

$$\mathcal{L}_1^B={\rm tr}\left[\bar{B}({\rm i}\gamma^\mu\nabla_\mu B-M_B)B\right]+\frac{D}{2}\,{\rm tr}\left(\bar{B}\gamma^\mu\gamma_5\,\{u_\mu,B\}\right)+\frac{F}{2}\,{\rm tr}\left(\bar{B}\gamma^\mu\gamma_5\,[u_\mu,B]\right),\tag{1.6}$$

where

$$\nabla_\mu B=\partial_\mu B+[\Gamma_\mu,B]\,,\tag{1.7}$$

$$\Gamma_\mu=\tfrac{1}{2}\left(u^\dagger\partial_\mu u+u\partial_\mu u^\dagger\right),\tag{1.8}$$

$$U=u^2=\exp\!\Big({\rm i}\sqrt{2}\Phi/f\Big)\tag{1.9}$$

$$u_\mu={\rm i}u^\dagger\partial_\mu U u^\dagger.\tag{1.10}$$

In chiral perturbation theory, the NG boson field adopts the SU(3) matrix representation

$$\Phi=\begin{pmatrix}\frac{1}{\sqrt{2}}\pi^0+\frac{1}{\sqrt{6}}\eta & \pi^+ & K^+\\ \pi^- & -\frac{1}{\sqrt{2}}\pi^0+\frac{1}{\sqrt{6}}\eta & K^0\\ K^- & \bar{K}^0 & -\frac{2}{\sqrt{6}}\eta\end{pmatrix},\tag{1.11}$$

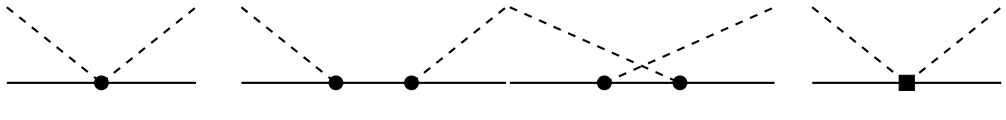

Figure 1.4. Feynman diagrams of chiral perturbation theory of the meson-baryon interaction. (a) Contact term of Weinberg-Tomozawa interaction, (b) Born term for the s-channel, contact term of the NLO interaction.

while the baryon field is

$$B = \begin{pmatrix} \frac{1}{\sqrt{2}}\Sigma^0 + \frac{1}{\sqrt{6}}\Lambda & \Sigma^+ & p \\ \Sigma^- & -\frac{1}{\sqrt{2}}\Sigma^0 + \frac{1}{\sqrt{6}}\Lambda & n \\ \Xi^- & \Xi^0 & -\frac{2}{\sqrt{6}}\Lambda \end{pmatrix}. \tag{1.12}$$

The schematic diagrams of the meson-baryon interaction are drawn in Fig. 1.4. To the lowest momentum order the corresponding interaction is given by the Weinberg-Tomozawa (WT) term. In this order the interaction Lagrangian adopts the form

$$\mathcal{L}_1^B = \frac{1}{4f^2}\,\mathrm{tr}\left(\bar{B}\mathrm{i}\gamma^\mu\left[\Phi\partial_\mu\Phi - (\partial_\mu\Phi)\Phi, B\right]\right), \tag{1.13}$$

whose corresponding diagram is shown in Fig. 1.4a. This Lagrangian will be used to obtain the $\bar{K}N$ scattering amplitude $T_{\bar{K}N}$ from which the $\bar{K}$-nucleus optical potential will be built, as we will show in Chapter 3.

1.3 Scattering theory

As has already been mentioned, the experimental study of the strong interaction is usually done through nuclear reactions. Experimentally, in these processes beams of different sort of particles —as leptons, bosons, hadrons or mesons— are made to collide with a target. In the experiments of our interest these targets are usually nuclei and, depending on the energy of the particles within the beam, the experiments can reveal different information of the structure of the particles involved.

At high energies, about the order of GeV, the particles of the beam are energetic enough to cross the nuclear barrier created by the target nucleus and penetrate it until collide with the nucleons. At these energies, the quark structure of the hadrons —as protons and neutrons— can be studied, since the energies involved are higher than the mass of the nucleons, ~ 939 MeV.

At lower energies, of the order of MeV, the particles of the beam cannot overcome the whole nuclear barrier. In this scenario, the particles with lower energy will interact only electromagnetically with the target nuclei suffering Coulomb scattering. On the other hand, the more energetic particles can overcome the nuclear barrier and get inside the range where the nuclear force is present. It is

in this scenario where the strong interaction can be analysed and where nuclear bound states of exotic particles can be formed.

The theoretical framework that treats this phenomena is called scattering theory and is introduced below.

In the quantum theory of a scattering process the wave function of the incident particle is expected to feel a perturbation just when is close enough to the target to interact through a potential V. That means that in the asymptotic limit, i.e. $r \to \pm\infty$ or $t \to \pm\infty$, the wave function of a particle can be approximated by a plane wave. Then, the wave function, which is solution of the Schrödinger equation, can be split into two terms,

$$\psi(\mathbf{r}) \xrightarrow[r\to\pm\infty]{} \psi_{\text{inc}}(\mathbf{r}) + \psi_{\text{scatt}}(\mathbf{r}), \tag{1.14}$$

where ψ_{inc} is the incoming plane wave of a particle of momentum $\mathbf{p}$ located at $\mathbf{r}$, i.e. $e^{\mathbf{i}\mathbf{p}\cdot\mathbf{r}}$, and ψ_{scatt} is the scattered wave function solution of the corresponding wave equation. Before solving the wave equation one can guess that the scattered wave function has a spherical form, then Eq. (1.14) might take the form of

$$\psi^{\pm}(\mathbf{r}) \xrightarrow[r\to\pm\infty]{} e^{\mathbf{i}\mathbf{p}\cdot\mathbf{r}} + f^{\pm}(p\mathbf{r}, \mathbf{p})\frac{e^{\pm \mathrm{i}\, pr}}{r}, \tag{1.15}$$

where $f^{\pm}(p\mathbf{r}, \mathbf{p})$ is the so-called "scattering amplitude" of the process, which weights the forward direction of the scattering wave function. The sign + refers to an "incoming" wave function and − to and "outgoing" one.

Then, the Hamiltonian H is decomposed in two parts $H = H_0 + V$, where H_0 is the free hamiltonian and V is the potential responsible of the scattering. For non-relativistic spinless particles $H_0 = \mathbf{p}/2m$ (Schrödinger), for relativistic spin-1/2 particles $H_0 = \boldsymbol{\alpha}\cdot\mathbf{p} + \beta m$ (Dirac) and for relativistic spin-0 particles $H_0^2 = \mathbf{p}^2 + m^2$ (Klein-Gordon) —as the mesons we are studying—.

In Hilbert space the wave equation reads

$$(H_0 + V)\left|\psi_a^{\pm}\right\rangle = E_a\left|\psi_a^{\pm}\right\rangle, \tag{1.16}$$

where E_a are the energy eigenvalues of the $|\psi_a^{\pm}\rangle$ eigenfunctions. If V is to be considered a perturbation the easier problem $V = 0$ can be solved and add V as a perturbation latter on. In this scenario the eigenvalue problem can be expressed as

$$(E_a - H_0)\left|\psi_a^{\pm}\right\rangle = V\left|\psi_a^{\pm}\right\rangle, \tag{1.17}$$

$$(E_a - H_0)\left|\phi_a\right\rangle = 0, \tag{1.18}$$

where $|\psi_a^{\pm}\rangle \to |\phi_a\rangle$ whenever $V = 0$. Solving for $|\psi_a^{\pm}\rangle$ one obtains

$$\left|\psi_a^{\pm}\right\rangle = |\phi_a\rangle + \frac{1}{E_a - H_0}V\left|\psi_a^{\pm}\right\rangle, \tag{1.19}$$

an equation known as Fredholm integral equation of second kind [38] which provides the scattered wave function of the scattering problem.

The fractional term in Eq. (1.19), i.e. $(E_a - H_0)^{-1}$, is known as the free *Green's function*, denoted as $G_0(E_a)$, and is usually interpreted as a term that brings the unperturbed initial state $|\phi_a\rangle$ to the final perturbed state $|\psi_a^{\pm}\rangle$ propagating it through the interaction V. Actually, it represents the loop that sums over all possible interaction between the particles. In coordinate space Eq. (1.19) reads

$$\left\langle \mathbf{r} \middle| \psi_a^{\pm} \right\rangle = \langle \mathbf{r} | \phi_a \rangle + \int \mathrm{d}^3 r' \left\langle \mathbf{r} \left| G_0(E_a) \right| \mathbf{r}' \right\rangle V(\mathbf{r}') \left\langle \mathbf{r}' \middle| \psi_a^{\pm} \right\rangle , \tag{1.20}$$

where it is assumed that the potential is local, i.e. $\langle \mathbf{r}' | V | \mathbf{r} \rangle = V(\mathbf{r}')\delta^{(3)}(\mathbf{r}' - \mathbf{r})$. This expression is related to the wave function decomposition that was done in Eq. (1.14), where the term under integral sign represents the scattered wave function ψ_{scatt}. Further, the term $G_0(\mathbf{r}, \mathbf{r}', E_a) \equiv \langle \mathbf{r} | G_0(E_a) | \mathbf{r}' \rangle$ is the expression of the Green function in coordinate space. In order to avoid divergences in Green's function the so-called "iε" description is used, therefore

$$G_0^{\pm}(E_a) = (E_a - H_0 \pm \mathrm{i}\varepsilon), \tag{1.21}$$

or for the total Hamiltonian

$$G^{\pm}(E_a) = (E_a - H \pm \mathrm{i}\varepsilon). \tag{1.22}$$

In the particular non-relativistic case, $H_0 = \mathbf{p}^2/2m$, in the momentums space $|\phi_a\rangle = |\mathbf{p}\rangle$, the operator H_0 is diagonal and thus $G_0(E_a)$ is also diagonal. By computing Green's function in coordinate space, $\langle \mathbf{r} | G_0(E_a) | \mathbf{r}' \rangle$, and introducing Eq. (1.15) in Eq. (1.20) one can solve for the scattering amplitude to get

$$f^{\pm}(\mathbf{p}', \mathbf{p}) = -\frac{2m}{4\pi} \int \mathrm{d}^3 r' e^{\mp \mathrm{i}\mathbf{p}'\cdot\mathbf{r}'} V(\mathbf{r}') \psi_a^{\pm}(\mathbf{r}') \tag{1.23}$$

$$= \left\langle \mathbf{p}' \left| V \right| \mathbf{p}^{\pm} \right\rangle , \tag{1.24}$$

where $\langle \mathbf{r} | \mathbf{p}^{\pm} \rangle = \psi_a^{\pm}$. At this point a redefinition is made to relate the scattering amplitude with the unperturbed states, that is

$$V \left| \mathbf{p}^{+} \right\rangle \equiv T \left| \mathbf{p} \right\rangle \tag{1.25}$$

which in Hilbert space reads

$$V \left| \psi_a^{+} \right\rangle = T \left| \phi_a \right\rangle , \tag{1.26}$$

where T is the so called T-matrix, which is of great importance in the calculations of the meson-nucleon optical potentials that are used in the present work. In turn, this redefinition let us write

$$f^{+}(\mathbf{p}', \mathbf{p}) = -\frac{m}{2\pi} \left\langle \mathbf{p}' \left| T \right| \mathbf{p} \right\rangle , \tag{1.27}$$

which relates the scattering amplitude of the process with the T-matrix.

Equation (1.19) already was a sort of integral Lippmann-Schwinger equation. It is most common to express it in terms of the T-matrix by using the definition in Eq. (1.25) and multiplying Eq. (1.19) by V from the left. Then, one obtains [39]

$$T(E) = V + VG_0^+(E)T(E). \tag{1.28}$$

Here E is a parameter that does not needed to be equal the energy of the plane-wave state. If the energies of the initial and final state are equal, i.e. $\mathbf{p}^2 = \mathbf{p}'^2$, it is said that the T-matrix is on the energy shell, otherwise is "off shell".

An interpretation of Eq. (1.28) can be obtained by substituting the $T(E)$ on the right side by the $T(E)$ of the left side to get a definition of $T(E)$ as an infinite series, that is

$$T(E) = V + VG_0^+(E)V + VG_0^+(E)VG_0^+(E)V + \cdots \tag{1.29}$$

In this expression we can see how the T-matrix takes account of all the possible interactions between particles —resummation— in a non-perturbative way.

The solution of Eq. (1.28) requires a self-consistent scheme to be solved, and is one of the main features of the different models discussed in this work, as we will see in the Chapter 3.

Chapter 2

Mesic Nuclear Bound States Formalism

A good decision is based on knowledge and not in numbers.

— Plato

Most of the part of this work has been the development of a code to compute nuclear quasi-bound states of different mesons —as K^-, $\bar{K}^0$ and η mesons— for different nuclei along the periodic table. In this chapter we explain the steps followed to solve our initial problem of the nuclear bound states.

The reader is kindly addressed to Ref. [40] —where the code is uploaded— to see the implementation of the algorithm.

2.1 The meson-nucleon formalism

The energy of a relativistic hadron, E, in the presence of a Coulomb, $V_{\rm C}$, and a nuclear, $U_{\rm N}$, fields is written as

$$E = \sqrt{\mathbf{p}_h^2 + m_h} + V_{\rm C} + U_{\rm N}, \tag{2.1}$$

where m_h is the hadron mass. Since $V_{\rm C}$ has scalar character [41] this equation is usually written as

$$(E - V_{\rm C})^2 = \left(\sqrt{\mathbf{p}_h^2 + m_h} + U_{\rm N}\right)^2 = \mathbf{p}_h^2 + m_h^2 + U_{\rm N}^2 + 2\sqrt{\mathbf{p}_h^2 + m_h}\, U_{\rm N}. \tag{2.2}$$

We are interested in the limit of small momenta, $|\mathbf{p}| \ll m_h$, and taking into account that quadratic terms in $U_{\rm N}$ are negligible we are left with

$$(E - V_{\rm C})^2 - \mathbf{p}_h^2 - m_h^2 - 2m_h U_{\rm N} = 0, \tag{2.3}$$

which is the Klein-Gordon equation dispersion relation of the problem.

In order to take account of the absorption of the meson in the nuclear medium $U_{\rm N}$ needs to be complex. In this approach the potential adopts the name of optical potential $V_{\rm opt}$. The real part of the optical potential gives information of the attractiveness of repulsiveness of the interaction while the

imaginary part encodes information about the absorption part of the potential. Thus, the eigenvalue $E \equiv \omega_h$ is also a complex value, which decompose as

$$\omega_h = m_h - \tilde{B}_h, \tag{2.4}$$

where $\tilde{B}_h = B_h + \mathrm{i}\Gamma_h/2$ being B_h is the binding of the energy of the hadron and Γ_h the width of the state.

The optical potential can be related with the self-energy (SE) of the hadron in the nuclear medium. As a first order approximations this relation is

$$2\,\mathrm{Re}(\omega_h)V_{\mathrm{opt}} = \Pi(\omega_h, \mathbf{p}, \rho(r)), \tag{2.5}$$

where $\rho(r) = \rho_p(r) + \rho_n(r)$ being $\rho_p(r)$ the proton density and $\rho_n(r)$ the neutron density profile, and q^μ is the quadrimomentum of the hadron.

Finally, remembering that the quantum operator of the momentum is $-i\nabla$ we can write the Klein-Gordon equation as

$$[\nabla^2 + (m_h - \tilde{B}_h - V_{\mathrm{C}})^2 - m_h^2 - \Pi(\omega_h, \mathbf{p}, \rho(r))]\psi = 0, \tag{2.6}$$

which describes the problem of hadron states under the presence of a Coulomb, V_{C}, and nuclear, U_{N}, fields.

2.2 Numerical solution of Klein-Gordon equation

To solve Eq. (2.6) first we have separated the wave function ψ in its radial and angular part, i.e.

$$\psi(\mathbf{r}) = \frac{u_{n\ell}(r)}{r} Y_{\ell m}(\theta, \phi). \tag{2.7}$$

and introducing it in Eq. (2.6) one gets the radial KG equation,

$$\frac{\mathrm{d}^2 u_{n\ell}(r)}{\mathrm{d}r^2} = -\left[(m_h - \tilde{B}_h - V_{\mathrm{C}}(r))^2 - m_h^2 - \Pi(\omega_h, \mathbf{p}, \rho(r)) - \frac{\ell(\ell+1)}{r^2}\right] u_{n\ell}(r). \tag{2.8}$$

It is important to stress that labels n, ℓ and m only refer to atomic states. In the case of the nuclear states these labels are dropped, as well as the centrifugal term $-\ell(\ell+1)/r^2$.

2.2.1 Numerov's method

Equation (2.8) is a second order differential equation which has no analytical solution. Thus, it should be solved numerically. For this purpose we have used *Numerov's method* [42], which considers a generic second order differential equation as

$$\frac{\mathrm{d}^2 u(x)}{\mathrm{d}x^2} = -g(x)u(x) + s(x), \tag{2.9}$$

where x is the spatial mesh where the integration is performed, and g and s are continuous functions within the mesh.

The first step in Numerov's method is to expand the solution function of Eq. (2.9) around a point x_n within the mesh in power series, that is

$$u_{n-1} = u_n - u'_n\Delta x + \tfrac{1}{2}y''_n(\Delta x)^2 - \tfrac{1}{6}u'''_n(\Delta x)^3 + \tfrac{1}{24}u_n^{(\mathrm{iv})}(\Delta x)^4 - \tfrac{1}{120}u_n^{(\mathrm{v})}(\Delta x)^5 + \mathcal{O}[(\Delta x)^6] \tag{2.10}$$

$$u_{n+1} = u_n + u'_n\Delta x + \tfrac{1}{2}y''_n(\Delta x)^2 + \tfrac{1}{6}u'''_n(\Delta x)^3 + \tfrac{1}{24}u_n^{(\mathrm{iv})}(\Delta x)^4 + \tfrac{1}{120}u_n^{(\mathrm{v})}(\Delta x)^5 + \mathcal{O}[(\Delta x)^6] \tag{2.11}$$

Summing both expressions (2.10) and (2.11) one gets rid of the terms with odd order derivatives to obtain

$$u_{n+1} + u_{n-1} = 2u_n + u''_n(\Delta x)^2 + \tfrac{1}{12}u_n^{(\mathrm{iv})}(\Delta x)^4 + \mathcal{O}[(\Delta x)^6]. \tag{2.12}$$

Further, if we express Eq. (2.9) in its discrete form, i.e.

$$u''_n = -g_n u_n + s_n \equiv h_n, \tag{2.13}$$

then, by analogy with Eq. (2.12), we can write

$$h_{n+1} + h_{n-1} = 2h_n + h''_n(\Delta x)^2 + \mathcal{O}[(\Delta x)^4]. \tag{2.14}$$

Undoing the change of variable one gets that the fourth derivative of u_n is

$$h''_n = u_n^{(\mathrm{iv})} = \frac{h_{n+1} - 2h_n + h_{n-1}}{(\Delta x)^2}. \tag{2.15}$$

Replacing this result in Eq. (2.12) we get

$$\begin{aligned} u_{n+1} = {} & 2u_n - u_{n-1} + (-g_n u_n + s_n)(\Delta x)^2 \\ & + \tfrac{1}{12}(-g_{n+1}u_{n+1} + s_{n+1} - 2(-g_n u_n + s_n) - g_{n-1}u_{n-1} + s_{n-1})(\Delta x)^2 \\ & + \mathcal{O}[(\Delta x)^6], \end{aligned} \tag{2.16}$$

and rearranging terms one finally gets

$$\begin{aligned} u_{n+1}\left[1 + g_{n+1}\tfrac{(\Delta x)^2}{12}\right] = {} & 2u_n\left[1 - 5g_n\tfrac{(\Delta x)^2}{12}\right] - u_{n-1}\left[1 + g_{n-1}\frac{(\Delta x)^2}{12}\right] \\ & + (s_{n+1} + 10s_n + s_{n-1})\tfrac{(\Delta x)^2}{12} + \mathcal{O}[(\Delta x)^6]. \end{aligned} \tag{2.17}$$

This Eq. (2.17) is know as Numerov's formula [42]. It solves Eq. (2.9) in the nodes of a mesh by giving the first two points u_n and u_{n-1}. The error of the approximation is of sixth order in Δx.

At this point we particularize Eq. (2.17) for our problem. The matching of Eq. (2.8) with Eq. (2.9) reveals that $s(x) = 0$ and

$$g(x) = (m_h - \tilde{B}_h - V_{\mathrm{C}}(x))^2 - m_h^2 - \Pi(\omega_h, \mathbf{p}, \rho(x)) - \frac{\ell(\ell+1)}{x^2}. \tag{2.18}$$

To make Eq. (2.17) more tractable is common to define

$$f_n \equiv 1 + g_n \frac{(\Delta x)^2}{12}, \tag{2.19}$$

which allows to write

$$u_{n+1} = \frac{(12 - 10f_n)u_n - f_{n-1}u_{n-1}}{f_{n+1}}, \tag{2.20}$$

that eases the coding procedure. Hence, by giving the starting points u_{-1} and u_0 one can obtain u_{n+1} along the whole mesh by iteration.

2.2.2 Numerical integration

Equation (2.8) is an eigenvalue problem in the complex plane in which the solution $u(r)$ exits —with its continuous requirements— for just a certain eigenvalue $\tilde{B}_h$. A typical way of solving these equations its by the so-called shooting method. This methods consists in trying a first guess eigenvalue $\tilde{B}_h$, then integrate the differential equation and check if the solution $u(r)$ fulfils the required continuity and the boundary conditions. If some of the conditions are not fulfilled the program tries another value until arriving to the one that solves the equation.

Continuity of the wave function

To solve the differential equation the boundary conditions must be set. In the following, we differentiate between the atomic and nuclear states:

i. *Atomic states*

In the case of mesic atoms the problem is treated by analogy to the hydrogen atom where the matching point is chosen to be the classical point turning of the particle, that is where the energy of the particle equals the potential energy. By analogy to the hydrogen atom, the energy spectrum is given by $E_\mu = -Z^2e^2/2n^2a_\mu$, then

$$-\frac{Z^2}{2n^2}\frac{e^2}{a_\mu} = -\frac{Ze^2}{r_\mathrm{t}} + \frac{\hbar^2}{2\mu}\frac{\ell(\ell+1)}{r_\mathrm{t}^2}, \tag{2.21}$$

where $\mu a_\mu = m_e a_0$ being a_0 the the Bohr radius and $\mu = m_h^{-1} + m_\mathrm{N}^{-1}$ the reduced mass of the meson-nucleus system. Solving for r_t the classical turning point is

$$r_\mathrm{match} \equiv r_\mathrm{t} = \frac{a_\mu}{Z}\left[n^2 + \sqrt{n^4 - n^2\ell(\ell+1)}\right]. \tag{2.22}$$

In the hydrogen-like atom this turning point is far from the nucleus and its surface —in the case of the hydrogen the nucleus is just a proton— since the wave function of the electron expands to distances relatively far from the nucleus and the wave function's tail hardly penetrates it. As we will

show latter, in the case of the mesic atoms this scenario changes. Since these particles are heavier, part of the tail of its wave function lies within the nucleus which enhance the effects of the strong interaction.

Besides, the boundary conditions are also the same ones as for the hydrogen atom. One is $u(0) = 0$ —which is a requirement when it is defined as in Eq. (2.7)— and the other $u(\infty) = 0$. Further, we already stressed that in order to solve numerically the differential equation using Numerov's method we have to give the first two points —or the last two points for the backwards integration— of the mesh. For this reason, we need the specify the behaviour of the wave functions at each limit. Also, by analogy to the well-known wave functions of the hydrogen atom, the expected behaviour of the atomic wave functions is

$$u_{\text{atom}}(r) \xrightarrow[r\to 0]{} r^{\ell+1}, \tag{2.23}$$

$$u_{\text{atom}}(r) \xrightarrow[r\to \infty]{} \exp(-Zr/na_\mu), \tag{2.24}$$

where ℓ is the angular quantum number of the atomic level. In our numerical calculation we set the numerical "infinity" at about ten times the nuclear radius, i.e. $\sim 10R_{\text{N}}$.

ii. *Nuclear states*

In the case of the nuclear states the wave function is much closer to the nucleus. Actually, it is expected that most of the part of the wave function lies within the nucleus. In this case the matching point is set to be the nuclear radius

$$r_{\text{match}} = r_0\, A^{1/3}, \tag{2.25}$$

where $r_0 \simeq 1.2$ fm and A is the number of nucleons in the nucleus.

The boundary conditions of our problem are the same as in the atomic levels, $u(0) = u(\infty) = 0$. From other studies of the nuclear states of meson particles, e.g. [43], the wave function falls off in a Gaussian-like form, but the behaviour at the origin remains the same as in the atomic level, that is

$$u_{\text{nuc}}(r) \xrightarrow[r\to 0]{} r^{\ell+1}, \tag{2.26}$$

$$u_{\text{nuc}}(r) \xrightarrow[r\to \infty]{} \exp\!\left(-r^2/R_{\text{N}}^2\right), \tag{2.27}$$

In this case the wave functions are expected to fall off to shorter distances than in the atomic states, thus we set the numerical "infinity" at $5R_{\text{N}}$.

To get the desired eigenvalue Eq. (2.8) is integrated in two direction: forward integration —from the origin to the matching point—; and backward integration —from "infinity" to the matching point—. The numerical calculation of both integrals —forward and backward— are independent of each other which might result in a different scaling of the corresponding wave functions. For that, the both wave functions must be forced to match at the matching point. At this stage it is important to stress that the solution $u(r)$ is a complex function

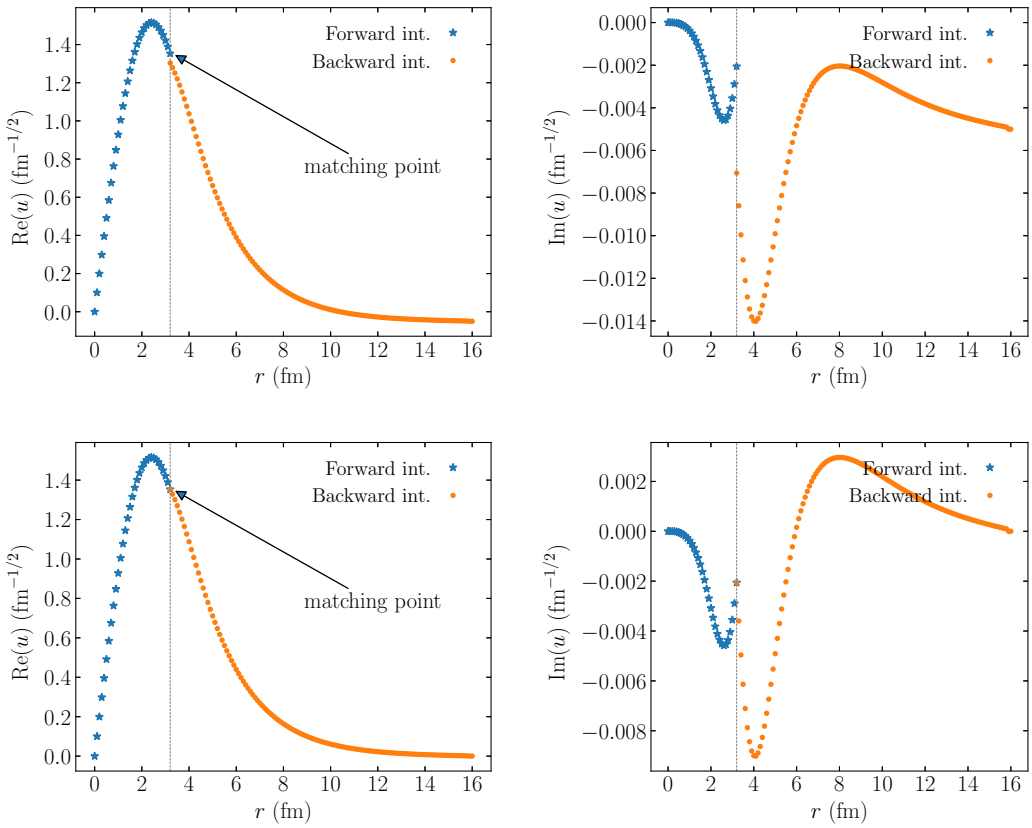

Figure 2.1. (Left) Real and (right) imaginary parts of the radial wave function. Wave functions without matching (up) and wave functions with matching (down). The graphic shows the forward integration (blue starts) and the backwards integration (orange dots) of Eq. (2.8) for a given self-energy and eigenvalue.

due to the fact that either the self-energy or the optical potential are complex functions. This fact requires a more detailed calculation than the usual one to solve the Schrödinger equation, thus we must have to into account that the continuity conditions must be fulfilled by both the real and imaginary parts of the wave function. This leads to the continuity condition of the wave function, i.e.

$$u_{\mathrm{m}}^{(\mathrm{F})} = \alpha \tilde{u}_{\mathrm{m}}^{(\mathrm{B})}, \tag{2.28}$$

where $u_{\mathrm{m}}^{(\mathrm{F})} = u^{(\mathrm{F})}(x_{\mathrm{m}})$ and $\tilde{u}_{\mathrm{m}}^{(\mathrm{B})} = \tilde{u}^{(\mathrm{B})}(x_{\mathrm{m}})$ refer to the forward and backward integrated wave function, respectively, at the matching point, and α is a scaling constant. Equation (2.28) can be expressed as

$$\mathrm{Re}\, u_{\mathrm{m}}^{(\mathrm{F})} + \mathrm{Im}\, u_{\mathrm{m}}^{(\mathrm{F})} = \alpha \left[\mathrm{Re}\, \tilde{u}_{\mathrm{m}}^{(\mathrm{B})} + \mathrm{Im}\, \tilde{u}_{\mathrm{m}}^{(\mathrm{B})}\right], \tag{2.29}$$

and to obtain the scaling constant one only needs to solve for α to get

$$\alpha = u_{\mathrm{m}}^{(\mathrm{F})} / \tilde{u}_{\mathrm{m}}^{(\mathrm{B})}, \tag{2.30}$$

Finally, to obtain the scaled wave function of, e.g., the backward integrated wave function one only needs to multiply $\tilde{u}^{(\mathrm{B})}(x)$ by α at each point of the

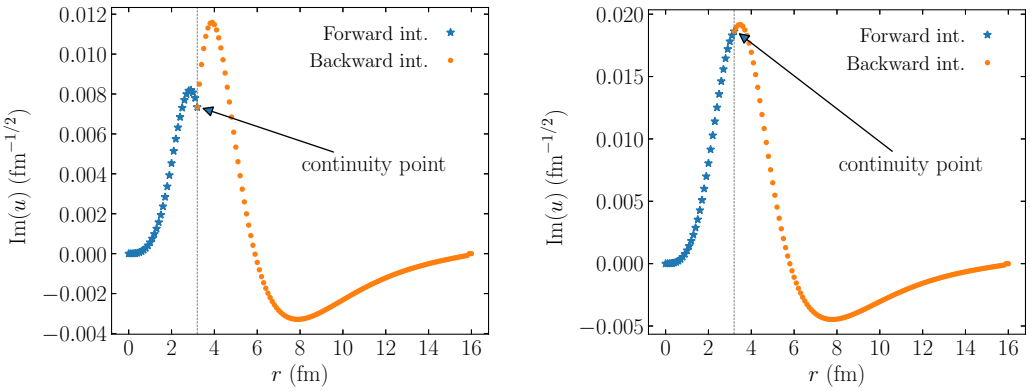

Figure 2.2. Imaginary parts of the radial wave function. The plot in the left shows the integrated wave functions without the continuity condition of the derivatives. In the right shows the same calculation for when the derivative continuity condition is implemented.

mesh to obtain $u^{(\mathrm{B})}(x)$ such that it is equal to $\alpha\tilde{u}^{(\mathrm{B})}(x)$ for all x within the integration mesh. This procedure is shown graphically in Fig. 2.1. There, one can appreciate the meaning of the scaling and its importance in the numerical calculation. Further, it is important to stress that this scaling process is crucial to obtain a correct and precise eigenvalue.

Looking at Fig. 2.1 one can see that there is still needed to impose the continuity of the derivatives of the wave function. For that, we chose to impose the continuity of the derivative of the wave function's logarithm at the matching point, i.e.

$$\frac{1}{u_{\mathrm{m}}^{(\mathrm{F})}}\left.\frac{\mathrm{d}u^{(\mathrm{F})}}{\mathrm{d}x}\right|_{x_{\mathrm{match}}} = \frac{1}{u_{\mathrm{m}}^{(\mathrm{B})}}\left.\frac{\mathrm{d}u^{(\mathrm{B})}}{\mathrm{d}x}\right|_{x_{\mathrm{match}}}, \tag{2.31}$$

what ensures the smooth continuity of the wave function. In Fig. 2.2 it is shown an example of this situation. The left-hand side plot shows the calculation performed with no requirements on the derivatives of the wave function. It is easy to see that the derivative of the wave function is not continuous at the matching point and hence this eigenvalue must be neglected asking to the program to look for another eigenvalue that improves the continuity of the derivative. On the other hand, the plot on the right shows the results of the calculation taking into account the continuity of the derivatives. In contrast to the plot in the left, the right-hand side plot reveals a smooth continuity of the wave functions from the forward integration and from the backward integration.

Steepest descent method

With the procedure described above one can integrate Eq. (2.8). However, the trial of random eigenvalues to solve the equation might lead to a long computational time or to a non-convergence of the calculations. Therefore, the code must look for by itself a new eigenvalue to perform a new calculation and check if all the above continuity conditions are fulfilled. For this reason we have implemented a *steepest descent method* routine. This procedure is no more that

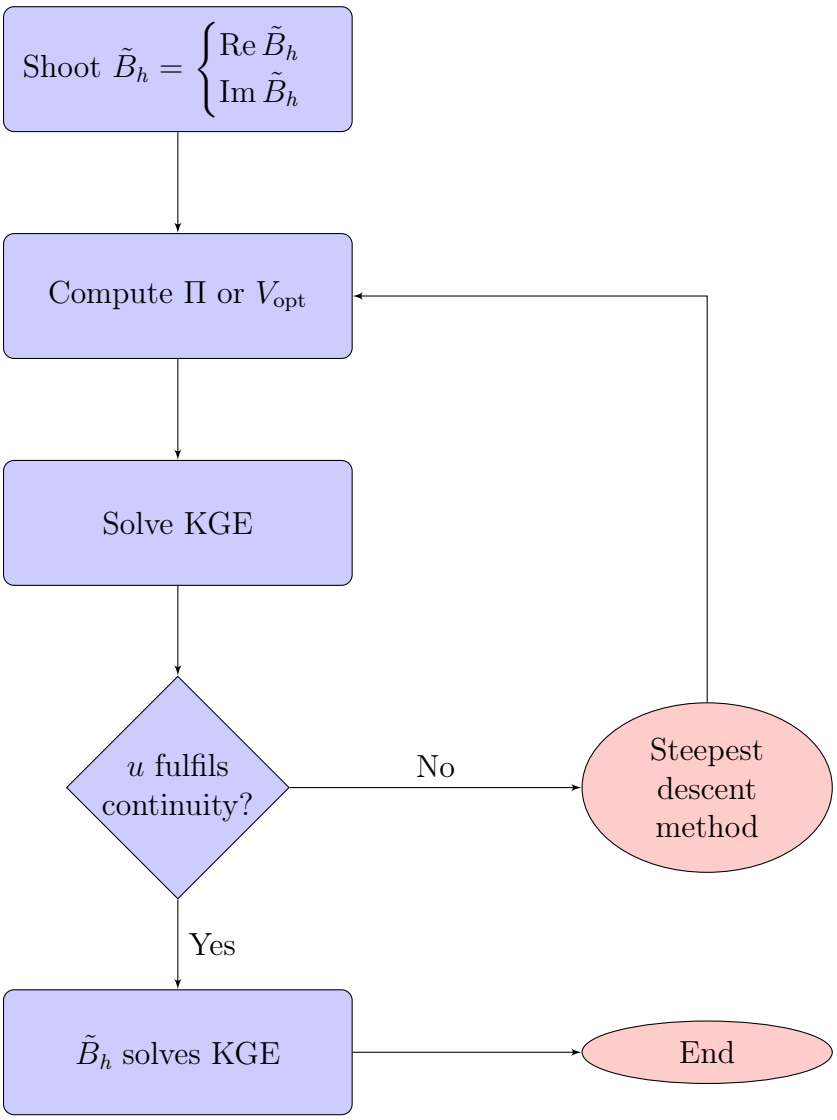

Figure 2.3. Flow diagram describing the steps followed to solve KG equation.

a gradient method that searches for a new eigenvalue such that the difference between derivatives decreases, that is

$$\left| \frac{u'^{(\mathrm{F})}_{\mathrm{m}}}{u^{(\mathrm{F})}_{\mathrm{m}}} - \frac{u'^{(\mathrm{B})}_{\mathrm{m}}}{u^{(\mathrm{B})}_{\mathrm{m}}} \right| \longrightarrow 0, \tag{2.32}$$

or which is the same,

$$G(\tilde{B}_h) \equiv \left| \frac{u'^{(\mathrm{F})}_{\mathrm{m}}}{u^{(\mathrm{F})}_{\mathrm{m}}} - \frac{u'^{(\mathrm{B})}_{\mathrm{m}}}{u^{(\mathrm{B})}_{\mathrm{m}}} \right|^{-1} \longrightarrow \infty. \tag{2.33}$$

Now the problem is left to maximize the function $G(\tilde{B}_h) \equiv G(x, y)$ where for the sake of brevity we define x and y as the real and imaginary parts, respectively, of $\tilde{B}_h$. Then, giving some initial conditions (x_0, y_0) the steepest descent method

states that the next set of values that maximizes G is given by

$$x = x_0 + \frac{G_x}{\|G\|}\Delta, \tag{2.34}$$

$$y = y_0 + \frac{G_y}{\|G\|}\Delta, \tag{2.35}$$

where Δ is a small variation step to perform the partial derivatives:

$$G_x = \frac{\partial G}{\partial x} \longrightarrow \frac{G(x_0 + \Delta, y_0) - G(x_0, y_0)}{\Delta}, \tag{2.36}$$

$$G_y = \frac{\partial G}{\partial y} \longrightarrow \frac{G(x_0, y_0 + \Delta) - G(x_0, y_0)}{\Delta}, \tag{2.37}$$

and

$$\|G\| = \sqrt{G_x^2 + G_y^2}. \tag{2.38}$$

The process described in Eqs. (2.34) and (2.35) is iterated until the correct eigenvalue $\tilde{B}_h = x + \mathrm{i}y$ is found. At this point, it is important to stress that Δ is a crucial parameter to obtain good values of the binding energy. In our calculations described below we varied Δ until we obtained the optimal value that lead to the convergence of the calculation.

To get a clearer idea of how te computation has to be performed Fig. 2.3 shows the flow diagram of the computational process. There we can see that the computation starts with "random" initial values for the real and imaginary part of the complex binding energy $\tilde{B}_h$. With this value for $\tilde{B}_h$ either the self-energy Π or the optical potential V_{opt} is computed —in the Chapter 3 this computations is explained in detail—. This gives all the parameters to solve the KG equation (2.8). Then, the solution of the KG equation, u, is studied to check if it fulfils the required continuity conditions for the derivatives between the forward and the backward integration parts. If these requirements are fulfilled then the complex binding energy shot in the first step is correct and the program stops. Otherwise, the program calls the steepest descent method routine that computes a new set of values for the real and imaginary parts of the complex binding energy to start again the the calculation of Π or V_{opt}. The process is iterated until the correct $\tilde{B}_h$ is found.

Chapter 3

$\bar{K}$ and η Nuclear Quasi-Bound States

There is in my opinion a great similarity between the problems provided by the mysterious behavior of the atom and those provided by the present economic paradoxes confronting the world.

— P. Dirac

The present chapter shows the result of the calculations explained in Chapter 2. We present the binding energies and widths of $\bar{K}$ and η nuclear states for different nuclei along the periodic table and for different models.

3.1 K^--atoms

Although the goal of this work is the study of nuclear bound states of mesons, it is interesting to first discuss the atomic states of these particles to latter on highlight the importance of going to the nuclear states to obtain more information about the strong interaction.

The interaction of mesons with the nucleus happens by two main processes: the electromagnetic interaction and the strong interaction. The electromagnetic interaction takes place only between the positively charged nucleus and negatively charged particles such as, e.g. π^-, K^-, $\bar{p}$ and Σ^-. Depending on the energy involved in the nuclear reactions one of the two interactions will dominate.

In the case of hadronic atoms the predominant interaction is the electromagnetic one. However, the experimental data of hadronic atoms is larger an easier to measure than that of hadronic nuclei. Hence, hadronic atoms provide a great scenario to study the strong interaction and the effects of the nuclear medium at zero kinetic energy [6]. In this work we focus in the strangeness sector $S = -1$ where the K^- belongs.

The important parameters in the study of hadronic atoms are the energy "shift", which is defined as the difference of the binding energy with respect to the purely electromagnetic level, that is

$$\varepsilon = B_{K^-} - B_{\mathrm{C}}, \tag{3.1}$$

where $B_{K^-} = \mathrm{Re}\,\tilde{B}_{K^-}$, and the "width", $\Gamma = 2\,\mathrm{Im}\,\tilde{B}_{K^-}$.

3.1.1 Optical potential for kaonic atoms

As has already been discussed before, we write the KG equation for K^- atoms as

$$\left[\nabla^2 + (\mu - \tilde{B}_{K^-} - V_{\mathrm{C}}(r))^2 - \mu^2 - 2\mu V_{\mathrm{opt}}\right]\psi = 0, \tag{3.2}$$

which differs with Eq. (2.3) in that we take into account the reduced mass of the meson-nucleus system instead of just the meson mass. The optical potential is approximated by

$$2\mu V_{\mathrm{opt}} = -4\pi\left(1 + \frac{\mu}{m_N}\right) f(0)\rho(r), \tag{3.3}$$

where $f(0)$ is the kaon-nucleon forward scattering amplitude and $m_N \simeq 939$ MeV is the nucleon mass. Equation (3.3) is known as $t\rho$ approximation and will by used systematically in this work.

Phenomenological potentials

For phenomenological potentials this forward scattering amplitude is replaced by a parameter b_0 which is fitted to the experimental data and the potential is called $t_{\mathrm{eff}}\rho$. In this work we use

$$b_0 = (0.52 \pm 0.03) + \mathrm{i}(0.80 \pm 0.03)\ \mathrm{fm}, \tag{3.4}$$

taken from [43], and we write the optical potential as

$$V_{\mathrm{opt}}^{(1)} = -4\pi\left(1 + \frac{\mu}{m_N}\right) b_0\rho(r). \tag{3.5}$$

This potential can, and shall, be improved in such a way that the scattering amplitude depends on the density in order to take into account the effects of the nuclear medium. This improvement is achieved by adding a density dependence

$$V_{\mathrm{opt}}^{(2)} = -4\pi\left(1 + \frac{\mu}{m_N}\right)\left[b_0^{\mathrm{exp}} + B_0\left(\frac{\rho(r)}{\rho_0}\right)^{\alpha}\right]\rho(r), \tag{3.6}$$

where $\rho_0 = 0.16$ fm, $b_0^{\mathrm{exp}} = -0.15 + \mathrm{i}0.62$ fm, $\alpha = 0.273 \pm 0.018$ and

$$B_0 = (1.62 \pm 0.04) + \mathrm{i}(-0.028 \pm 0.009)\ \mathrm{fm}, \tag{3.7}$$

are experimental values obtained from fits to the available data.

Theoretical potentials

In contrast to the phenomenological potentials, theoretical potentials have been developed for the $\bar{K}$ in the nuclear medium, as the one in Refs. [37, 44]. There,

	K^-p	$\bar{K}^0n$	$\pi^0\Lambda$	$\pi^0\Sigma^0$	$\eta\Lambda$	$\eta\Sigma^0$	$\pi^+\Sigma^-$	$\pi^-\Sigma^+$	$K^+\Xi^-$	$K^0\Xi^0$
K^-p	2	1	$\frac{\sqrt{3}}{2}$	$\frac{1}{2}$	$\frac{3}{2}$	$\frac{\sqrt{3}}{2}$	0	1	0	0
$\bar{K}^0n$		2	$-\frac{\sqrt{3}}{2}$	$\frac{1}{2}$	$\frac{3}{2}$	$-\frac{\sqrt{3}}{2}$	1	0	0	0
$\pi^0\Lambda$			0	0	0	0	0	0	$\frac{\sqrt{3}}{3}$	$-\frac{\sqrt{3}}{2}$
$\pi^0\Sigma^0$				0	0	0	2	2	$\frac{1}{2}$	$\frac{1}{2}$
$\eta\Lambda$					0	0	2	2	$\frac{3}{2}$	$\frac{3}{2}$
$\eta\Sigma^0$						0	0	0	$\frac{\sqrt{3}}{2}$	$-\frac{\sqrt{3}}{2}$
$\pi^+\Sigma^-$							2	0	1	0
$\pi^-\Sigma^+$								2	0	1
$K^+\Xi^-$									2	1
$K^0\Xi^0$										2

Table 3.1. Matrix coefficients $C_{ij} = C_{ji}$ of V_{ij} amplitude.

a non-perturbative model in coupled channels has been developed employing the lowest-order chiral Lagrangian —Eq. (1.13)— where a resummation is performed over all Feynman diagrams in the s-channel. The model includes Pauli blocking to take into account the states occupied by the other nucleons an the $\bar{K}$ self-energy.

Free space amplitude

The free-space model reproduces successfully the $\Lambda(1405)$ resonance and takes into account the 10 possible channels for the K^-p scattering, i.e.

$$K^-p \to K^-p, \bar{K}^0n, \pi^0\Lambda, \pi^0\Sigma^0, \pi^+\Sigma^-, \pi^-\Sigma^+, \eta\Lambda, \eta\Sigma^0, K^+\Xi^-, K^0\Xi^0. \tag{3.8}$$

Using the Lagrangian of Eq. (1.13) one can derive that the potential amplitude describing these scattering processes is given by

$$V_{ij} = -C_{ij}\frac{1}{4f^2}\bar{u}(p_i)\gamma^\mu u(p_j)\left(k_{i,\mu} + k_{j,\mu}\right), \tag{3.9}$$

where $p_{j,i}$ and $k_{j,i}$ are the final, initial momenta of baryons and mesons, respectively. In the limit of low energies the spatial component of the momenta can be neglected and we can rewrite Eq. (3.9) as

$$V_{ij} = -C_{ij}\frac{1}{4f^2}\left(k_j^0 + k_i^0\right), \tag{3.10}$$

where the C_{ij} coefficients are listed in Table 3.1.

With this V_{ij} amplitude, the Lippman-Schwinger —or Bethe-Salperter— equation can be written as

$$T_{ij} = V_{ij} + \overline{V_{i\ell}G_\ell T_{\ell j}}, \tag{3.11}$$

where T_{ij} is the T-matrix of the ij channel and G_ℓ the Green function introduced in Chapter 2, and the sub-indices i, ℓ and j run over all the channels described

above. The over-line over the last term in Eq. (3.11) stands for the resummation over all possible Feynman diagrams in the s-channel and reads [37]

$$\overline{V_{i\ell}G_\ell T_{\ell j}} = \mathrm{i}\int \frac{\mathrm{d}^4q}{(2\pi)^4}\frac{M_\ell}{E_\ell(-\mathbf{q})}\frac{V_{i\ell}(k_i,q)T_{\ell j}(q,k_j)}{\sqrt{s}-q^0+E_\ell(-\mathbf{q})+\mathrm{i}\varepsilon}\frac{1}{q^2-m_\ell^2+\mathrm{i}\varepsilon}, \tag{3.12}$$

where M_ℓ is the baryon mass, $E_\ell(-\mathbf{q})$ the baryon energy and m_ℓ the mass of the meson in the intermediate state. Reference [44] justifies that the off-shell amplitudes can be factorized leaving the loop integral as

$$G_\ell(\sqrt{s}) = \mathrm{i}\int \frac{\mathrm{d}^4q}{(2\pi)^4}\frac{M_\ell}{E_\ell(-\mathbf{q})}\frac{1}{\sqrt{s}-q^0-E_\ell(-\mathbf{q})+\mathrm{i}\varepsilon}\frac{1}{q^2-m_\ell^2+\mathrm{i}\varepsilon} \tag{3.13}$$

$$= \int_{|\mathbf{q}|<q_{\max}} \frac{\mathrm{d}^3q}{(2\pi)^3}\frac{1}{2\omega_\ell(\mathbf{q})}\frac{M_\ell}{E_\ell(-\mathbf{q})}\frac{1}{\sqrt{s}-\omega_\ell(\mathbf{q})-E_\ell(-\mathbf{q})+\mathrm{i}\varepsilon}, \tag{3.14}$$

where $\sqrt{s}=p^0+k^0$, $\omega_\ell(\mathbf{q})$ is the energy of the meson and $q_{\max}=630$ MeV [37] is the cut-off of the regularization loop.

In-medium amplitude

The previous model predicts a repulsive averaged amplitude $\overline{T}$ of the K^-p, K^-n scattering. However, the available data of kaonic atoms show an attractive potential for the K^- even for small nuclear densities, far below ρ_0. This means that in order to reproduce the K^- properties the density dependence of the T-matrix must be included explicitly by setting $\overline{T}\to T(\rho)$. Defining the total momentum $\mathbf{P}=\mathbf{p}_N+\mathbf{p}_{K^-}$ in the laboratory frame, where $\mathbf{p}_N$ is the nucleon momentum in the Fermi sea and $\mathbf{p}_{K^-}$ the momentum of K^-, one can use the previous formalism by replacing the free propagator by the in-medium propagator —in the lab frame—, i.e.

$$\begin{aligned} G_\ell(P^0,\mathbf{P},\rho) =& \mathrm{i}\int \frac{\mathrm{d}^4q}{(2\pi)^4}\frac{M_\ell}{E_\ell(-\mathbf{q})}\left[\frac{1-n(\mathbf{q}_{\rm lab})}{\sqrt{s}-q^0-E_\ell(-\mathbf{q})+\mathrm{i}\varepsilon}\right. \\ &\left.+\frac{n(\mathbf{q}_{\rm lab})}{\sqrt{s}-q^0-E_\ell(-\mathbf{q})+\mathrm{i}\varepsilon}\right]\frac{1}{q^2-m_\ell^2-\Pi_{\bar{K}}^{(s)}(q^0,\mathbf{q},\rho)}, \end{aligned} \tag{3.15}$$

where $P^\mu=(P^0,\mathbf{P})$ it he total four-momentum in the lab frame, the Mandelstam variable $s=(P^0)^2-\mathbf{P}^2$ and

$$\mathbf{q}_{\rm lab} = \left[-\left(\frac{P^0}{\sqrt{s}}-1\right)\frac{\mathbf{P}\cdot\mathbf{q}}{|\mathbf{P}|^2}+\frac{\sqrt{s}-q^0}{\sqrt{s}}\right]\mathbf{P}-\mathbf{q} \tag{3.16}$$

is the momentum of the nucleon in the lab frame that corresponds to a momentum $-\mathbf{q}$ in the center of mass frame.

In this scenario, in Ref. [37] they compute the $\bar{K}$ self-energy for the s-wave as

$$\Pi_{\bar{K}}^{(s)}(q^0,\mathbf{q},\rho) = 2\int\frac{\mathrm{d}^3p}{(2\pi)^3}n(\mathbf{p})\left[T_{\bar{K}p}(P^0,\mathbf{P},\rho)+T_{\bar{K}n}(P^0,\mathbf{P},\rho)\right], \tag{3.17}$$

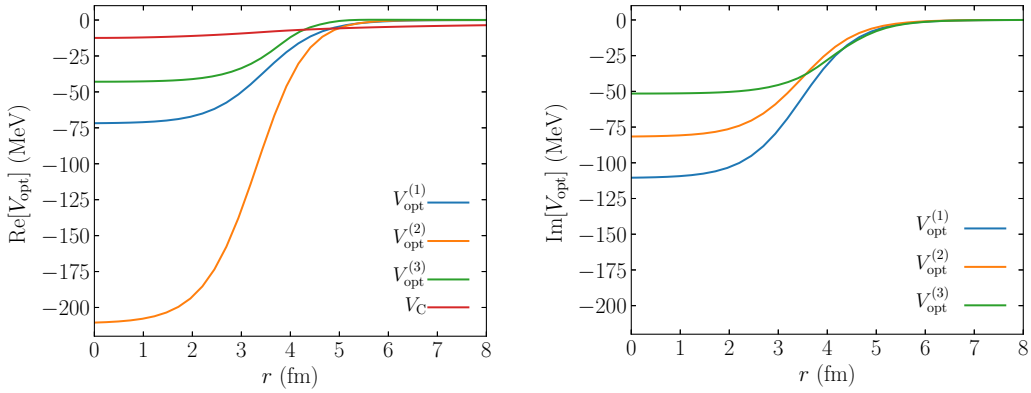

Figure 3.1. (Left) Real and (right) imaginary parts of the phenomenological, label (1), phenomenological density-dependent, label (2), and chiral theory based, label (3), optical potentials for the ^{40}Ca nucleus. Also, the Coulomb potential is plotted.

where $q^\mu = (q^0, \mathbf{q})$ is the $\bar{K}$ four-momentum, $P^0 = q^0 + E(\mathbf{p})$ the total energy and $\mathbf{P} = \mathbf{q} + \mathbf{p}$ the total momentum in the lab frame. Finally, the purely theoretical potential taken from [37, 44] is labelled and defined as

$$2\mu V_{\rm opt}^{(3)} = \Pi_{K^-}^{(s)}(q^0, \mathbf{q}, \rho), \tag{3.18}$$

being $\Pi_{K^-}^{(s)}(q^0, \mathbf{q}, \rho)$ the K^- self-energy.

3.1.2 Kaonic atoms energy shifts and widths

We used our program code to compute the energy shifts and widths of K^- atomic states for different nuclei along the periodic table. The solutions of our calculations are shown in Tables 3.2 and 3.3. There, we specify the nucleus, the atomic level computed and the shifts, $\varepsilon = B_{K^-} - B_{\rm C}$, and widths, Γ, of the level. To compute the shifts we solved the KG equation twice, one with the optical potential switched off, $V_{\rm opt}^{(i)} = 0$, to obtain $B_{\rm C}$, and other with the optical potential switched on to obtain B_{K^-}. Then, ε_i measures the displacement of the purely electromagnetic atomic level by the action of the strong interaction. With these definitions, negative values of the shifts mean a repulsive effect of the strong potential and positive values an attractive effect.

Studying Table 3.2 we see that all the shifts are negative, which means that the effect of the strong interaction in the atomic levels is repulsive meaning that the levels are less bound when the strong interaction is taken into account. Besides, we can see that the overall results obtained with the three different potentials are similar, although the depth of the potentials is quite different, as we can see from Fig. 3.1, which shows the optical potential of the $\bar{K}N$ interactions in ^{40}Ca. The purely theoretical potential $V_{\rm opt}^{(3)}$ shows a maximum depth of ~ 45 MeV, while the phenomenological ones $V_{\rm opt}^{(1)}$ and $V_{\rm opt}^{(2)}$ have the maximum depth at ~ 70 MeV and ~ 220 MeV, respectively. In the case of the imaginary part, the potential $V_{\rm opt}^{(1)}$ shows now the biggest depth of ~ 110 MeV, followed by $V_{\rm opt}^{(2)}$ with ~ 80 MeV and finally $V_{\rm opt}^{(3)}$ with ~ 50 MeV. This explains

Nucleus	Level	ε_1	ε_2	ε_3	$\varepsilon_{\rm exp}$
^{7}Li	2p	-0.014	-0.022	-0.017	0.002 ± 0.026
^{9}Be	2p	-0.069	-0.102	-0.088	-0.079 ± 0.021
^{10}B	2p	-0.225	-0.245	-0.265	-0.208 ± 0.035
^{11}B	2p	-0.240	-0.226	-0.291	-0.167 ± 0.035
^{12}C	2p	-0.636	-0.565	-0.758	-0.590 ± 0.080
^{16}O	3p	-0.010	-0.010	-0.009	-0.025 ± 0.018
^{24}Mg	3d	-0.039	-0.041	-0.095	-0.027 ± 0.015
^{27}Al	3d	-0.068	-0.081	-0.172	-0.080 ± 0.013
^{28}Si	3d	-0.125	-0.152	-0.288	-0.139 ± 0.014
^{31}P	3d	-0.265	-0.337	-0.535	-0.330 ± 0.080
^{32}S	3d	-0.439	-0.568	-0.838	-0.494 ± 0.038
^{35}Cl	3d	-0.896	-1.110	-1.504	-1.00 ± 0.17
^{59}Co	4f	-0.107	-0.160	-0.294	-0.099 ± 0.106
^{58}Ni	4f	-0.139	-0.204	-0.370	-0.223 ± 0.042
^{63}Cu	4f	-0.243	-0.343	-0.574	-0.370 ± 0.047
^{108}Ag	5g	-0.260	-0.346	-0.567	-0.18 ± 0.12
^{112}Cd	5g	-0.360	-0.470	-0.749	-0.40 ± 0.10
^{115}In	5g	-0.458	-0.591	-1.003	-0.53 ± 0.15
^{228}Sn	5g	-0.568	-0.718	-1.271	-0.41 ± 0.18
^{165}Ho	6h	-0.185	-0.255	-0.522	-0.30 ± 0.13
^{208}Pb	7i	-0.023	-0.034	-0.098	-0.020 ± 0.012
^{238}U	7i	-0.139	-0.209	-0.538	-0.26 ± 0.4

Table 3.2. Energy shifts (ε_i) in keV of K^--atomic levels for different nuclei along the periodic table computed with potential V_i for $i = 1, 2$ and 3.

that in our calculation we obtained, in most of the cases, that the narrower widths are due to the purely theoretical potential, which has the less deep imaginary part. Comparing these depths with the atomic level widths in Table 3.3 we see that in most of the cases the deeper the imaginary part of the optical potential the bigger the width and the smaller the magnitude of the energy shift.

These results reveal that K^- atomic levels are not really sensitive neither to the nuclear potential nor to the depth of the real part of the optical potential. Therefore, in order to get more information about the $\bar{K}N$ interaction we have to study the interaction at shorter distances, where the strong interaction dominates and nuclear bound or quasi-bound states can be formed.

3.2 $\bar{K}$-nuclei

We saw that the theoretical study of kaonic atoms let us reproduce most of the available experimental data. However, the calculations do no depend strongly

Nucleus	Level	Γ_1	Γ_2	Γ_3	$\Gamma_{\rm exp}$
^{7}Li	2p	0.044	0.042	0.031	0.055 ± 0.029
^{9}Be	2p	0.260	0.234	0.214	0.172 ± 0.058
^{10}B	2p	0.706	0.594	0.626	0.810 ± 0.100
^{11}B	2p	0.694	0.632	0.631	0.700 ± 0.080
^{12}C	2p	1.601	1.571	1.500	1.730 ± 0.150
^{16}O	3p	0.000	0.000	0.000	0.017 ± 0.014
^{24}Mg	3d	0.278	0.259	0.226	0.214 ± 0.015
^{27}Al	3d	0.491	0.513	0.412	0.443 ± 0.022
^{28}Si	3d	0.819	0.867	0.688	0.801 ± 0.032
^{31}P	3d	1.438	1.515	1.193	1.440 ± 0.120
^{32}S	3d	2.183	2.285	0.018	2.187 ± 0.103
^{35}Cl	3d	3.636	3.771	2.934	2.91 ± 0.24
^{59}Co	4f	0.843	0.853	0.720	0.64 ± 0.25
^{58}Ni	4f	1.077	1.099	0.901	1.03 ± 0.12
^{63}Cu	4f	1.584	1.580	1.305	1.37 ± 0.17
^{108}Ag	5g	1.578	1.566	1.332	1.54 ± 0.58
^{112}Cd	5g	2.029	2.003	1.696	2.01 ± 0.44
^{115}In	5g	2.699	2.634	2.205	2.38 ± 0.57
^{228}Sn	5g	3.403	3.315	2.743	3.18 ± 0.64
^{165}Ho	6h	1.484	1.465	1.224	2.14 ± 0.31
^{208}Pb	7i	0.263	0.261	0.240	0.37 ± 0.15
^{238}U	7i	1.551	1.534	1.268	1.50 ± 0.75

Table 3.3. Level widths (Γ_i) in keV of K^--atomic levels for different nuclei along the periodic table computed with potential V_i for $i = 1, 2$ and 3.

on the depth of the potential —i.e. in the model used—, which forces to look for different approaches to obtain new information about the strong interaction. The importance of the depth of the K^- nuclear potential arises when studying K^- nuclear clusters [45], multistrange self-bound matter [46] and compact starts, since it determines the possibility of having these scenarios.

On the other hand, neutral mesons —as $\bar{K}^0$ and η— are of great interests in these studies since only the strong interaction takes place. In this section we study the nuclear states of antikaos, $\bar{K}$, in the nuclear medium. The theoretical framework in which we performed the calculations belongs to the work of [37, 44] already discussed for the kaonic atoms.

3.2.1 Antikaon scattering amplitudes

Figure 3.2 shows the $\bar{K}$ scattering T-matrix computed in a in-medium chiral motivated calculation in [37, 44]. In order to make an intuitive meaning of the

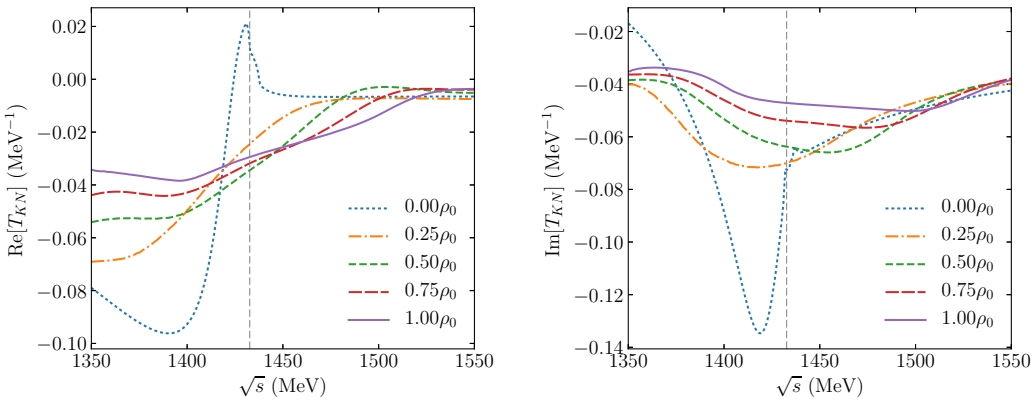

Figure 3.2. (Left) Real and (right) imaginary parts of the $\bar{K}$ scattering T-matrix from [37] for different fractions of the nuclear density $\rho_0 = 0.16$ fm^{-3}.

quantity $T_{\bar{K}N}$, it can be related with the scattering amplitude $F_{\bar{K}N}$ by

$$T_{\bar{K}N}(\sqrt{s},\rho) = -4\pi\frac{\sqrt{s}}{E_N}F_{\bar{K}N}(\sqrt{s},\rho), \tag{3.19}$$

where $\sqrt{s}$ is the total energy in the center of mass frame (c.m.), ρ the nuclear density and E_N the energy of the nucleon.

Although the formalism has already been discussed in the previous section for the kaonic atoms it is interesting to reformulate some equations in terms of the important parameters for the nuclear states. To begin with, we started we the $\bar{K}$ potential in nuclear matter density [47]

$$V_{\bar{K}} = -\frac{2\pi}{\omega_{\bar{K}}}\left(1+\frac{\omega_{\bar{K}}}{m_N}\right)F_{\bar{K}N}(\sqrt{s},\rho)\rho, \tag{3.20}$$

where $\omega_{\bar{K}}$ is the $\bar{K}$ meson energy, $m_N \simeq 939$ MeV the nucleon mass. An important quantity here is the Mandelstam variable

$$s = (E_{\bar{K}} + E_N)^2 - (\mathbf{p}_{\bar{K}} + \mathbf{p}_N)^2, \tag{3.21}$$

where $E_{\bar{K}(N)}$ and $\mathbf{p}_{\bar{K}(N)}$ is the energy and momentum of the meson (nucleon) in the laboratory frame. It is important to point out some remarks about Eq. (3.21). Previous works on the topic —Refs. [47, 48]— consider the following approximation:

$$E_{\bar{K}} = \sqrt{m_{\bar{K}}^2 + \mathbf{p}_{\bar{K}}^2} + \mathrm{Re}\,U_{\bar{K}}(r) \simeq m_{\bar{K}} + \frac{\mathbf{p}_{\bar{K}}^2}{2m_{\bar{K}}} + \mathrm{Re}\,U_{\bar{K}}(r) = m_{\bar{K}} - B_{\bar{K}} \tag{3.22}$$

$$E_N = \sqrt{m_N^2 + \mathbf{p}_N^2} + U_N(r) \simeq m_N + \frac{\mathbf{p}_N^2}{2m_N} + U_N(r) = m_N - B_N \tag{3.23}$$

where $U_{\bar{K}} = V_{\bar{K}} + V_{\rm C}$ and $B_{\bar{K}(N)}$ are the meson (nucleon) binding energies. Introducing this information in Eq. (3.21) and doing the square root one obtains

$$\sqrt{s} = \sqrt{(m_{\bar{K}} + m_N - B_{\bar{K}} - B_N)^2 - (\mathbf{p}_{\bar{K}} + \mathbf{p}_N)^2} \leq \sqrt{s_{\rm th}}, \tag{3.24}$$

where $\sqrt{s_{\rm th}} = m_{\bar{K}} + m_N$. This result is crucial to understand the result of this work since $\mathbf{p}_{\bar{K}} + \mathbf{p}_N = 0$ in the c.m. frame but $\mathbf{p}_{\bar{K}} + \mathbf{p}_N \neq 0$ in the lab frame. The fact of having non-zero nucleon momentum is a direct consequence of taking into account the presence of the nuclear medium. Thus, this momentum term that is subtracting the energy part of Eq. (3.24) is producing a shift to $\sqrt{s}$, forcing it to lie below the energy threshold $\sqrt{s_{\rm th}}$. This is an important result since the amplitude $T_{\bar{K}N}(\sqrt{s}, \rho)$ has to be computed at *subthreshold* energies. Looking at Fig. 3.2 we see that at subthreshold energies $T_{\bar{K}N}$ is, in general, attractive and the probability of finding nuclear quasi-bound states increases.

On the other hand, the average of the momentum term can be developed as

$$\left\langle (\mathbf{p}_{\bar{K}} + \mathbf{p}_N)^2 \right\rangle = \mathbf{p}_{\bar{K}}^2 + \mathbf{p}_N^2, \tag{3.25}$$

where the term $\mathbf{p}_{\bar{K}} \cdot \mathbf{p}_N \to 0$ since the direction of the nucleon momentum in the nucleus, $\mathbf{p}_N$, shall be averaged over all the directions in the space. This allows to write

$$\sqrt{s} = m_{\bar{K}} + m_N - B_{\bar{K}} - B_N - \frac{m_N}{m_{\bar{K}} + m_N} \frac{\mathbf{p}_N^2}{2m_N} - \frac{m_{\bar{K}}}{m_{\bar{K}} + m_N} \frac{\mathbf{p}_{\bar{K}}^2}{2m_{\bar{K}}} \tag{3.26}$$

Finally, approximating the kinetic energy of the nucleon to the one in a Fermi sea,

$$\frac{\mathbf{p}_N^2}{2m_N} = T_N \left(\frac{\rho}{\rho_0} \right)^{2/3}, \tag{3.27}$$

where $T_N = 23.0$ MeV, and the kinetic energy of the meson in the local density approximation —directly form Eq. (3.22)— for the antikaon

$$\frac{\mathbf{p}_{\bar{K}}^2}{2m_{\bar{K}}} = -B_{\bar{K}} - \mathrm{Re}\, U_{\bar{K}}, \tag{3.28}$$

where $U_{\bar{K}} = V_{\bar{K}} + V_{\rm C}$ for K^- and $U_{\bar{K}} = V_{\bar{K}}$ for $\bar{K}^0$. Therefore, the total energy in the c.m. can be rewritten as

$$\sqrt{s} - V_{\rm C} = m_{\bar{K}} + m_N - B_N - \frac{m_N}{m_{\bar{K}} + m_N} B_{\bar{K}} - 15.1 \left(\frac{\rho}{\rho_0} \right)^{2/3} + \frac{m_{\bar{K}}}{m_{\bar{K}} + m_N} \mathrm{Re}\, U_{\bar{K}}(\rho). \tag{3.29}$$

This expression is the one used in previous works as in Refs. [47, 48]. However, in this work we propose our own prescription of $\sqrt{s}$. For the antikaon energy we us the same approximation as in Eq. (3.22) from which we can solve for the momentum

$$\mathbf{p}_{\bar{K}}^2 = (E_{\bar{K}} - \mathrm{Re}\, U_{\bar{K}})^2 - m_{\bar{K}}^2 \simeq (m_{\bar{K}} - B_{\bar{K}} - \mathrm{Re}\, U_{\bar{K}})^2 - m_{\bar{K}}^2. \tag{3.30}$$

Nucleus	B_{K^-}	Γ_{K^-}	$\sqrt{s_{K^-N}}$
^{12}C	15.70	73.34	1388.5
^{24}Mg	25.77	72.10	1385.8
^{32}S	29.79	80.27	1382.4
^{40}Ca	32.78	82.55	1379.0
^{208}Pb	30.73	65.81	1378.6

Table 3.4. Binding energies, widths and energy in the c.m. for K^- nuclear states in different nuclei.

Nucleus	$B_{\bar{K}^0}$	$\Gamma_{\bar{K}^0}$	$\sqrt{s_{\bar{K}^0N}}$
^{12}C	10.04	76.07	1394.2
^{24}Mg	19.13	73.05	1392.5
^{32}S	22.17	80.41	1390.1
^{40}Ca	24.35	81.26	1387.5
^{208}Pb	35.13	85.79	1381.8

Table 3.5. Binding energies, widths and energy in the c.m. for $\bar{K}^0$ nuclear states in different nuclei.

For the nucleon we use also the same approximation as in Eq. (3.23) and the same kinetic energy for a Fermi gas model, but we use a linear dependence in ρ for the nucleon potential in the nuclear medium, i.e.

$$U_N(r) = U_0 \, \frac{\rho}{\bar{\rho}} \, \text{MeV}, \tag{3.31}$$

where $U_0 = -50$ MeV and $\bar{\rho}$ is the normalization constant of the density such that

$$\int \mathrm{d}^3 r \rho(r) = A. \tag{3.32}$$

With these recipes we write our Mandelstam variable as

$$\begin{aligned} s = & \left[m_{\bar{K}} - B_{\bar{K}} + m_N + T_N \left(\frac{\rho}{\rho_0} \right)^{2/3} + U_0 \frac{\rho}{\bar{\rho}} \right]^2 \\ & - (m_{\bar{K}} - B_{\bar{K}} - U_{\bar{K}}(\sqrt{s}, \rho))^2 + m_{\bar{K}}^2 - 4 m_N^2 T_N^2 \left(\frac{\rho}{\rho_0} \right)^{4/3}, \end{aligned} \tag{3.33}$$

whose square root is the quantity used in our calculations.

3.2.2 Antikaon binding energies and widths

To compute the binding energies of the $\bar{K}$ nuclear quasi-bound states we solved KG equation as explained in Chapter 3. In this particular case the KG equation is written as

$$\left[\nabla^2 + (m_{\bar{K}} - \tilde{B}_{\bar{K}} - V_{\mathrm{C}})^2 - m_{\bar{K}}^2 - \Pi_{\bar{K}}(\sqrt{s}, \rho) \right] \psi = 0, \tag{3.34}$$

where $\tilde{B}_{\bar{K}} = B_{\bar{K}} + \mathrm{i}\Gamma_{\bar{K}}/2$, V_{C} is only activated for K^- and

$$\Pi_{\bar{K}}(\sqrt{s}, \rho) \simeq T_{\bar{K}N}(\sqrt{s}, \rho)\rho. \tag{3.35}$$

where

$$T_{\bar{K}N} = \tfrac{1}{2}(t_{\bar{K}p} + t_{\bar{K}n}), \tag{3.36}$$

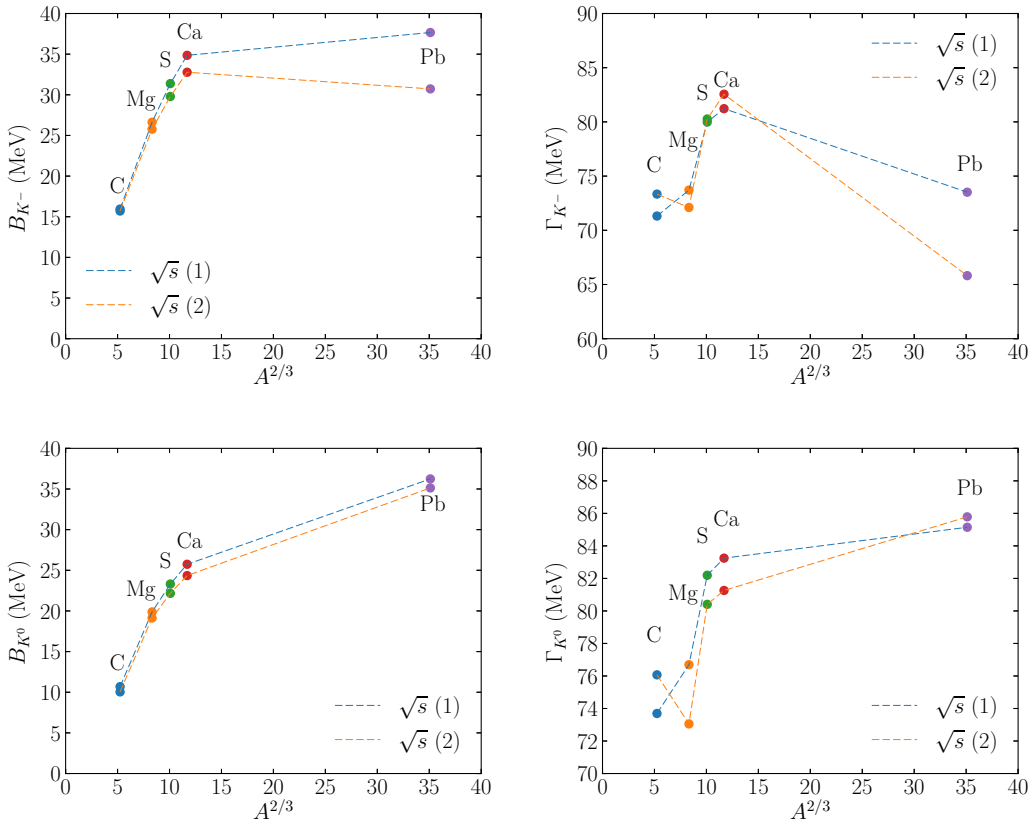

Figure 3.3. (Up) K^- (bottom) $\bar{K}^0$ calculations. (Left) Binding energies and (right) widths of nuclear states levels for different nuclei computed with the scattering $T_{\bar{K}N}$ plotted in Fig. 3.2. Both graphs show the calculations for different $\sqrt{s}$ prescriptions: $\sqrt{s}$ (1) stands for prescription in Eq. 3.29 and $\sqrt{s}$ (2) for our prescription in Eq. 3.33.

being $t_{\bar{K}p}$ and $t_{\bar{K}n}$ the proton and neutron contributions to the amplitude.

To perform the calculation it is important to take into account the $\sqrt{s}$ and ρ dependence of the quantities. We see that the KG equation (3.34) contains, by Eq. (3.35), $T_{\bar{K}N}$, which depends on $\sqrt{s}$ and ρ. From the square root of Eq. (3.33) we see that $\sqrt{s}$ also depends on ρ and on $V_{\bar{K}}(\rho)$, which in turn, from Eq. (3.20), depends on $T_{\bar{K}N}$ and thus on $\sqrt{s}$. This presents a scenario in which the KG equation must be solved in a self-consistent way in order to compute $\sqrt{s}$ for each point in the mesh. An schematic flow diagram is shown in Fig. 3.4 showing the self-consistent algorithm to compute the scattering amplitude at each point of the mesh, which is an extension to the previous flow diagram shown in Fig. 2.3.

The results of these calculations are shown in Tables 3.4 for K^--nuclei and 3.5 for $\bar{K}^0$-nuclei, where we present the nucleus for which the calculations is performed, the binding energy, $B_{\bar{K}}$, and width, $\Gamma_{\bar{K}}$, of the level, and the c.m. energy $\sqrt{s}$. We recall that the $\sqrt{s_{\rm th}} \simeq 1435$ MeV, hence the first thing to notice is that all the values of the c.m. energy fulfil $\sqrt{s} \leq \sqrt{s_{\rm th}}$ as expected from our definition of s in Eq. (3.21).

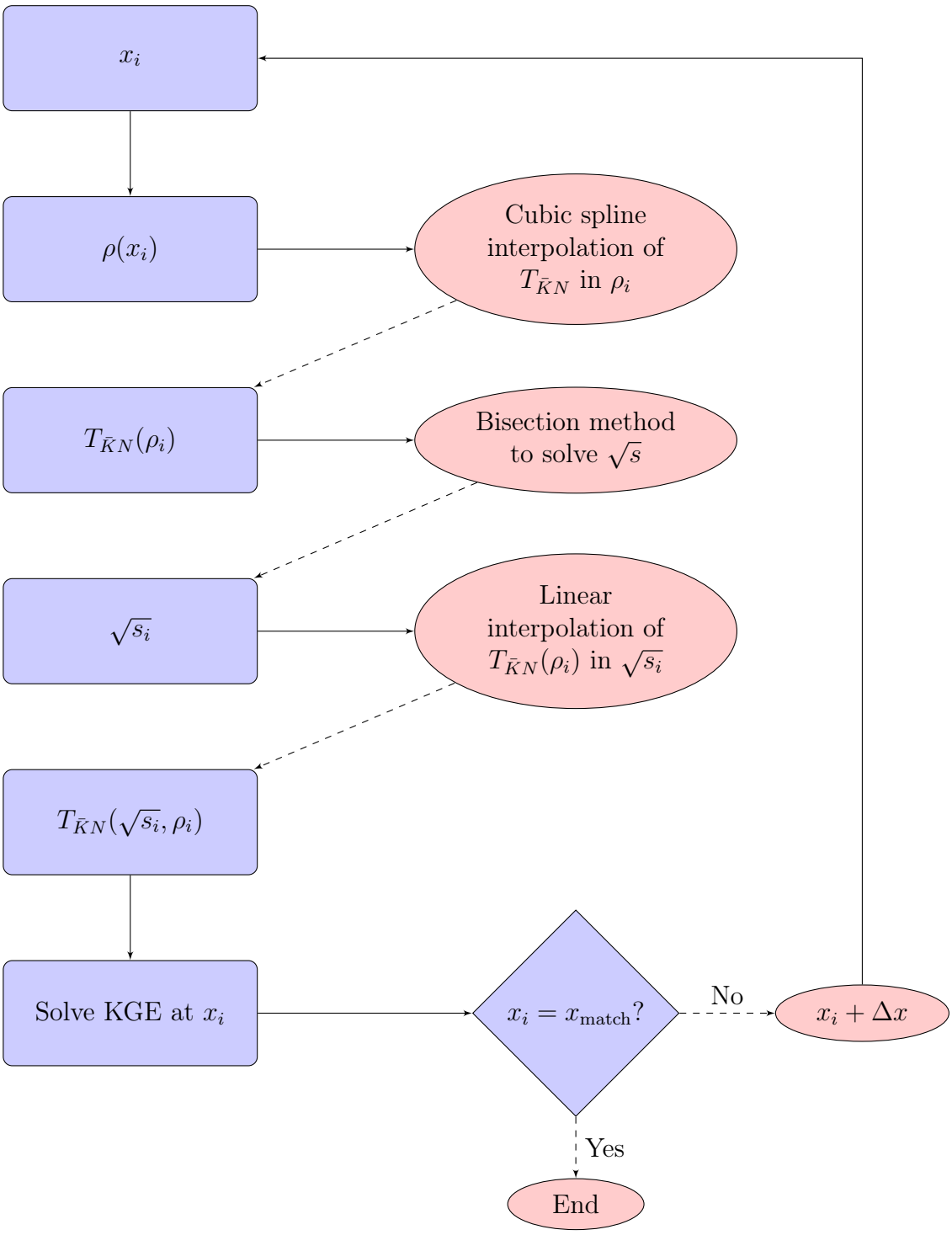

Figure 3.4. Flow diagram describing the steps followed to compute the scattering amplitudes in a self-consistent way with $\sqrt{s}$.

Studying the binding energies and widths we see first that these results predict quasi-bound states of K^- and $\bar{K}^0$ —since we defined $B_{\bar{K}} > 0$ for bound states—. The term quasi-bound is related to the non-zero width of the level. These widths are usually —at least for the calculations made to this date— much greater than the binding energies, what broadens the level to values where

$B_{\bar{K}} < 0$, a condition where the particles are unbound. When comparing K^- with $\bar{K}^0$ nuclear states we see that the levels for K^- are always more bound that the ones for $\bar{K}^0$. This is partly because of the presence of the Coulomb field that attracts negatively charged mesons towards the nucleus.

To see the behaviour of these nuclear states, the data in Tables 3.4 and 3.5 are plotted in the upper and bottom parts of Fig. 3.3, respectively. There, we also plot the same calculation made for the $\sqrt{s}$ prescription in Eq. (3.29) —labelled as $\sqrt{s}$ (1)— used in previous works as in Ref. [47]. The behaviour of the binding energy is similar for both prescriptions. In the case of the K^- results the difference of binding energies between prescriptions increases for heavier nuclei. Actually, with our prescription Eq. (3.33) —labelled as $\sqrt{s}$ (2) in Fig. 3.3— the binding energy turns out to be smaller for the ^{208}Pb than for the ^{40}Ca as well as the width of the level. On the other hand, the calculated $\bar{K}^0$ binding energies are quite the same for all nuclei, and so do the widths, which only show slight deviations from one prescription to the other for certain nuclei.

3.3 η-nuclei

For the study of η nuclear quasi-bound states we followed a similar procedure as in the case of $\bar{K}$ nuclear levels. In this case we study the nuclear quasi-bound states of five different models for the ηN interaction, namely: CS [50], GW [51], IOV [52], KSW [53] and M2 [54] —all five already discussed in Refs. [48, 49]—. For the case of the CS model we also study the η nuclear quasi-bound states employing the ηN scattering amplitude in the nuclear medium, that is $F_{\eta N}$ at $\rho = \rho_0$.

All the ηN models considered are based in coupled-channel calculations that reproduce dynamically the baryon $N^*(1535)$ resonance, which lies around 50 MeV over the ηN threshold, $\sqrt{s_{\eta N}}_{\rm th} = m_\eta + m_N \simeq 1487$ MeV. However, as will be shown latter, the scattering amplitudes of the ηN interaction are strongly model dependent.

3.3.1 η scattering amplitudes

The scattering amplitudes in free-space of different models used in this work are plotted in Fig. 3.5. We notice that the qualitative features of the scattering amplitudes in free-space for all five different models are similar. The real part of the ηN scattering amplitude $F_{\eta N}(\sqrt{s})$ at $\rho = 0$ has its maximum at threshold. Above threshold, the scattering amplitudes decrease until becoming, in all cases, negative. The maximum value of the imaginary part of the scattering amplitudes is closely related with the $N^*(1535)$ resonance. It is remarkable that the position of the peak is above threshold, in contrast to the one of the $\bar{K}$ scattering amplitude where the $\Lambda(1405)$ resonance appears below the $\bar{K}N$ threshold. This means that the influence of the $N^*(1535)$ resonance in our in-medium η results will be more moderate than that for the $\bar{K}$ mesons, because we will also explore subthreshold energies, as we show in our Table 3.6, where the $\sqrt{s_{\eta N}}$ are now further away from the resonant structure.

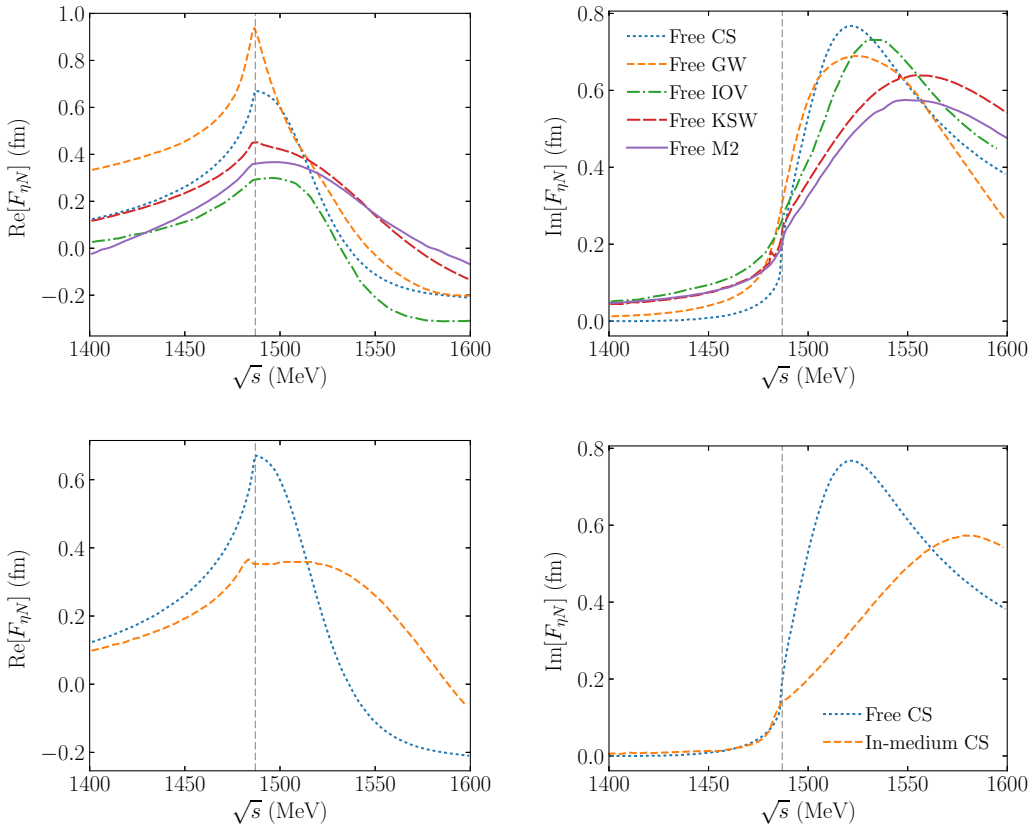

Figure 3.5. Up: (Left) Real and (right) imaginary parts of the ηN scattering amplitude $F_{\eta N}(\sqrt{s})$ in the free-space as a function of $\sqrt{s}$ for the models CS, GW, IOV, KWS and M2. Bottom: Scattering amplitudes for the CS model in the free-space and in the nuclear medium $\rho_0 = 0.17$ fm^{-3}.

Further, the bottom part of Fig. 3.5 shows the scattering amplitudes for the CS model in free-space and in the nuclear medium at $\rho_0 = 0.17$ fm^{-3}. One can notice that the real part of the scattering amplitude in the nuclear medium is smaller, at subthreshold, than the free-space one. In the case of the imaginary part the peak is displaced to higher values of $\sqrt{s}$ above threshold at the same time that it is smoothed showing a wider and less sharper peak than in the free-space scenario. However, as has already been mentioned, the relevant part for the η nuclear quasi-bound states is the subthreshold domain, and the imaginary part of $F_{\eta N}(\sqrt{s})$ has a similar behaviour for the free-space and for the nuclear medium, falling off rapidly for subthreshold values of the total c.m. energy. Thus we expect similar values of the energy level width for the calculations with the free-space and the nuclear-medium CS model scattering amplitudes, although the results might differ due to the different value of the $\sqrt{s}$ employed in each case.

(a) Free CS model

Nucleus	B_η	Γ_η	$\sqrt{s_{\eta N}}$
^{12}C	5.85	1.62	1456.7
^{24}Mg	7.11	0.99	1459.5
^{32}S	9.63	0.99	1458.4
^{40}Ca	10.39	0.87	1457.0
^{208}Pb	14.14	0.39	1455.7

(b) Nuclear medium CS model

Nucleus	B_η	Γ_η	$\sqrt{s_{\eta N}}$
^{12}C	2.38	1.89	1461.1
^{24}Mg	3.97	1.68	1463.0
^{32}S	5.98	2.01	1462.2
^{40}Ca	6.71	2.00	1460.9
^{208}Pb	10.59	1.92	1459.1

(c) Free GW model

Nucleus	B_η	Γ_η	$\sqrt{s_{\eta N}}$
^{12}C	15.12	5.03	1445.8
^{24}Mg	18.27	3.71	1449.7
^{32}S	23.25	3.91	1446.7
^{40}Ca	24.61	3.74	1444.9
^{208}Pb	30.18	3.04	1442.9

(d) Free IOV model

Nucleus	B_η	Γ_η	$\sqrt{s_{\eta N}}$
^{12}C	-1.41	9.96	1465.6
^{24}Mg	-0.43	8.92	1466.9
^{32}S	0.71	12.12	1466.8
^{40}Ca	1.27	12.69	1465.6
^{208}Pb	4.52	14.63	1464.0

(e) Free KWS model

Nucleus	B_η	Γ_η	$\sqrt{s_{\eta N}}$
^{12}C	3.79	9.53	1459.0
^{24}Mg	5.54	8.86	1461.2
^{32}S	8.00	10.78	1460.1
^{40}Ca	8.85	10.93	1458.7
^{208}Pb	13.06	10.98	1456.9

(f) Free M2 model

Nucleus	B_η	Γ_η	$\sqrt{s_{\eta N}}$
^{12}C	0.61	8.36	1463.1
^{24}Mg	1.50	7.38	1465.0
^{32}S	2.87	9.66	1464.7
^{40}Ca	3.35	10.03	1463.5
^{208}Pb	5.95	11.43	1462.4

Table 3.6. Binding energies, level widths and total c.m. energy for the different models and different nuclei.

3.3.2 η binding energies and widths

To compute the binding energies of the η nuclear bound states we follow the same steps as in the previous section. Now, the KG equation is written as

$$\left[\nabla^2 + (m_\eta - \tilde{B}_\eta)^2 - m_\eta^2 - \Pi_\eta(\sqrt{s}, \rho)\right] \psi = 0, \tag{3.37}$$

where $\tilde{B} = B_\eta + \mathrm{i}\Gamma_\eta$, $m_\eta \simeq 548$ MeV is the mass of the η and the self-energy

$$\Pi_\eta(\sqrt{s}, \rho) = 2\omega_\eta V_\eta = -4\pi \frac{\sqrt{s}}{E_N} F_{\eta N}(\sqrt{s}, \rho)\rho, \tag{3.38}$$

with $\omega_\eta = m_\eta - B_\eta$. In our calculations we use our proposed prescription for $\sqrt{s}$ as in Eq. (3.33). In the particular case of the η it reads

$$s = \left[m_\eta - B_\eta + m_N + T_N \left(\frac{\rho}{\rho_0} \right)^{2/3} + U_0 \frac{\rho}{\bar{\rho}} \right]^2 - \left(m_\eta - B_\eta - V_\eta(\sqrt{s}, \rho) \right)^2 + m_\eta^2 - 4 m_N^2 T_N^2 \left(\frac{\rho}{\rho_0} \right)^{4/3} . \tag{3.39}$$

The algorithm followed to solve the KG equation for the η nuclear quasi-bound states is the same as we explained for the $\bar{K}$ nuclear levels. The scattering amplitudes in Fig. 3.5 have to be interpolated and $\sqrt{s}$ has to be solved self-consistently for each point in the mesh.

The results of our calculations are shown in Table 3.6. For a better analysis of these results, the data are also plotted in Fig. 3.6. In the case of the CS model, we see that the binding energies are, approximately, in a range between 6–15 MeV for the calculation with the free-space scattering amplitude and between 2–10 MeV for the nuclear medium scattering amplitude. Besides, the most interesting part of these result are the widths of the levels. The values of the widths range around 0.3–2 MeV for both the free-space and the nuclear medium calculation, which are much smaller than the binding energies. The ratio of the widths with respect to the binding energies, i.e. Γ_η / B_η, goes from 3% for the minimum to 30% for the maximum. However, a proper calculation would require to take into account the in-medium effects, i.e. computing $F_{\eta N}(\sqrt{s}, \rho)$ for each values of the density ρ —as we did with the $\bar{K}$ nuclear quasi-bound states—. Either way, we expect that the calculation with the in-medium scattering amplitude gives binding energies and widths in between the ones computed for the free-space scattering amplitude at $\rho = 0$ and for the nuclear medium one at $\rho = \rho_0$. In this scenario we can talk about nuclear bound states and no about nuclear quasi-bound states, since —theoretically— this levels could be experimentally resolved.

For the other models we obtain different results. In the case of the GW model the binding energies are more than twice the ones of the CS model. However, the widths are also small in comparison with the binding energies, the ratio of the widths with respect to the binding energies range over 10 to 30%.

The other models present a different scenario. For the case of the IOV model the calculated binding energies are much smaller than in the previous cases. Actually, for the ^{12}C and ^{24}Mg the binding energies are negative, which means that a bound state cannot be formed. Besides, the widths are bigger than the binding energies and the ratio Γ_η / B_η is much greater than the unity in all the cases. The M2 model shows a similar behaviour. Although in this model all calculations give $B_\eta > 0$ and the widths of the levels are also much higher — twice or three times— than the binding energies.

Finally, slightly better result are obtained for the KWS model. The binding energies are more similar to the ones of the CS model —in particular for the

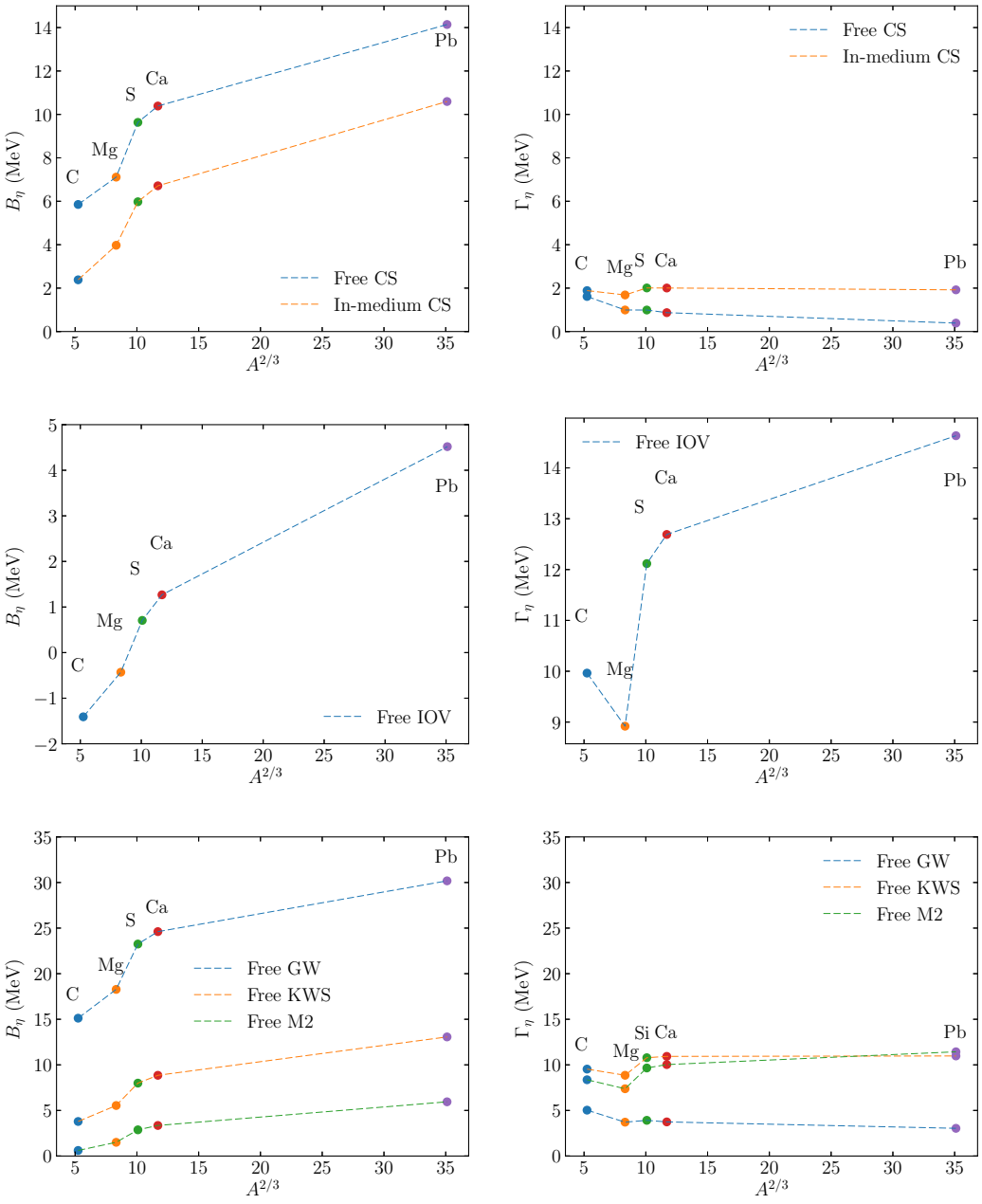

Figure 3.6. (Left) Binding energies and (right) widths of η-nuclear states levels for different nuclei computed for different models. Top: CS model for free-space and nuclear medium; middle: IOV model in free-space; bottom: GW, KWS and M2 models in free-space.

nuclear medium results—. However, the widths are also bigger than the binding energies of the nuclear quasi-bound states.

The result of these calculations can be explained by studying the scattering amplitudes of each model in Fig. 3.5. For example, the imaginary scattering amplitude of the CS and GW models in the free-space fall off faster —for decreasing values of $\sqrt{s}$— than the other models. Actually, the smaller widths are due to the CS model which is the one that falls of faster followed by the GW model which predicts the next smaller widths. The imaginary part of the scattering amplitudes of the KSW and M2 models almost overlap at subthrehold, what justify the similarity in their calculated widths. Finally, the scattering amplitude of the free-space IOV model is the one that falls off more slowly and, consequently, the one that predicts larger values of the widths of the nuclear levels.

As a last comment on these result, looking at the values of $\sqrt{s_{\eta N}}$ in Table 3.6 —that gives the values that solve Eq. (3.39)— we see that all of them are below the threshold of 1487 MeV. This agrees with our previous expectation that the relevant part of the scattering amplitudes for the η nuclear quasi-bound states is the one below threshold.

Chapter 4

Summary

There are two possible outcomes: if the result confirms the hypothesis, then you've made a measurement; if the result is contrary to the hypothesis, then you've made a discovery.

— E. Fermi

In this work we have calculated the binding energies of the nuclear quasi-bound states of mesons in the strangeness $S = -1$ sector, K^-, $\bar{K}^0$, and of the η mesons. For this purpose we developed a code to solve the Klein-Gordon equation describing the problem. This code implements several options to compute the nuclear binding energies, B_h, and widths, Γ_h, of $\bar{K}$ and η mesons for a wide variety of nuclear —optical— potentials based on different theoretical models. The purpose of this study has been to bring about some information on whether these mesons are able or not to form nuclear quasi-bound states in order to provide some information on the properties of the meson-baryon interaction.

In the case of the K^- we first reviewed the atomic states that these particles can create when interacting electromagnetically with the nucleus. In contrast to the $\bar{K}^0$ and η mesons the K^- has negative charge. This means that, even at long distances, where the range of the strong interaction vanishes or it is small, K^- mesons can form atomic bound states due to the Coulomb interaction with the nucleus. We saw that the energy shifts —or displacements of the purely electromagnetic binding energies by the action of the strong interaction— were rather small for both the phenomenological and theoretical potentials used. Besides, the computed widths of the levels, were rather big in comparison with the binding energies. However, we noticed that, although the results did not depend strongly on the model used, they were not conclusive in determining the depth of the $\bar{K}$-nucleus optical potential. For this reason we stepped forward to study the nuclear states of the $\bar{K}$ and η mesons.

For the study of the nuclear quasi-bound states of antikaons $\bar{K}$ we performed calculations for a chiral motivated model based on the lowest-order meson-baryon chiral Lagrangian in s-wave. The amplitudes $T_{\bar{K}N}$ were influenced by the presence of the $\Lambda(1405)$ resonance at subthreshold with a tendency to disappear for increasing values of the nuclear density. The $\bar{K}$-nucleus optical potential required computing the amplitude $T_{\bar{K}N}(\sqrt{s}, \rho)$ for each value

of the nuclear density $\rho(r)$. At this point we should remark that the exigence of the calculation increased notably when comparing with the calculation of the atomic states. Further, we took into account the energy dependence, of the scattering amplitude at subthreshold energies, introducing a new prescription for $\sqrt{s}$ and performing our calculations in a self-consistent way to solve the KG equation. The results showed positive values of the binding energies and large values of the widths of the nuclear states. These results gave us important information about the $\bar{K}N$ interaction: first that it can bind $\bar{K}$ mesons in nuclei, although the states would be highly unstable, and second, a strong energy and density dependence at subthrehold energies, what stresses the dominant effect of the $\Lambda(1405)$ below threshold.

We also studied η nuclear bound and quasi-bound states for five different ηN chirally motivated interaction models. All the models studied reproduce the $N^*(1535)$ baryon resonance above threshold, but present a quite different behaviour at subthreshold energies. The computational procedure of this calculation was quite similar to the one for the $\bar{K}$ mesons and a bit less exigent since the nuclear medium has not been taken into account self-consistently when computing the scattering amplitudes. In relation with the results obtained for the binding energies and widths we observed several facts. On the one hand, we saw that some of the models, as the IOV, KWS and M2, produced widths with similar values to the binding energies. This led us to refer to them as η nuclear quasi-bound states. On the other hand, we saw that the CS model —the one that include meson self-energies self-consistently— produces η nuclear binding energies much higher than the widths of the levels. This is a quite important result since these models predict realistic scenarios where experimental evidences of these systems can be measured. However, we recall that these results are strongly model dependent, both for the binding energies and the widths.

As a final note we would like to stress that studying meson bound states in nuclei serves as a link between the theory and the experiment. Nuclear bound states can be measured in nuclear reactions, and have been the goal of several experiments. By comparing the theoretical predictions for the binding energies and widths with the experiments, the issue of the model dependence shown in this work can be overcome by rejecting the results that do not fit the experimental data, smoothing the path for a better understanding of the strong interaction.

Bibliography

[1] E. Fermi, E. Teller, Phys. Rev. **72** (1947) 399.

[2] J. A. Wheeler, Phys. Rev. **71** (1947) 320.

[3] M. Conversi et al., Phys. Rev. **71** (1947) 209.

[4] C. J. Batty, Sov. J. Part. Nucl. 13 (1982) 71.

[5] M. Camac et al., Phys. Rev. **99** (1955) 905.

[6] C. J. Batty, E. Friedman, A. Gal, Phys. Rep. **286** (1997) 385.

[7] V. Metag, M. Nanova, E. Ya. Paryev, Prog. Part. and Nucl. Phys. **97** (2017) 199.

[8] W. Scheinast, et al., Phys. Rev. Lett. **96** (2006) 072301.

[9] P. Crochet, et al., Phys. Lett. B **486** (2000) 6.

[10] M. Büscher, et al., Eur. Phys. J. A **22** (2004) 301.

[11] P. Srisawad, et al., J. Phys. Conf. Ser. **509** (2014) 012034.

[12] V. Zinyuk, et al., Phys. Rev. C **90** (2014) 025210.

[13] M.L. Benabderrahmane, et al., Phys. Rev. Lett. 102 (2009) 182501.

[14] G. Agakishiev, et al., Phys. Rev. C **82** (2010) 044907.

[15] G. Agakishiev, et al., Phys. Rev. C **90** (2014) 054906.

[16] Yu.T. Kiselev, et al., Phys. Rev. C **92** (2015) 065201.

[17] T. Kishimoto, et al., Nuclear Phys. A **827** (2009) 321c.

[18] M. Roebig-Landau, et al., Phys. Lett. B **373** (1996) 45.

[19] J.J. Xie, et al., Phys. Rev. C **95** (2017) 015202.

[20] M. Nanova, et al., Phys. Lett. B **710** (2012) 600.

[21] S. Friedrich, et al., Eur. Phys. J. A **52** (2016) 297.

[22] M. Nanova, et al., Phys. Lett. B **727** (2013) 417.

[23] M. Nanova, et al., Phys. Rev. C **94** (2016) 025205.

[24] M. Kotulla, et al., Phys. Rev. Lett. **100** (2008) 192302; Phys. Rev. Lett. **114** (2015) 199903.

[25] V. Metag, Hyperfine Interact. **234** (2015) 25.

[26] S. Friedrich, et al., Phys. Lett. B **736** (2014) 26.

[27] M. Naruki, et al., Phys. Rev. Lett. **96** (2006) 092301.

[28] M. Wood, et al., Phys. Rev. C **78** (2008) 015201.

[29] A. Polyanskiy, et al., Phys. Lett. B **695** (2011) 74.

[30] M. Hartmann, et al., Phys. Rev. C **85** (2012) 035206.

[31] M.H. Wood, et al., Phys. Rev. Lett. **105** (2010) 112301.

[32] T. Ishikawa, et al., Phys. Lett. B **608** (2005) 215.

[33] R. Muto, et al., Phys. Rev. Lett. **98** (2007) 042501.

[34] Y. Nambu, G. Jona-Lasinio, Phys. Rev. **122** (1961) 345.

[35] Y. Nambu, G. Jona-Lasinio, Phys. Rev. **124** (1961) 246.

[36] J. Goldstone, Nuovo Cim. **19** (1961) 154.

[37] À. Ramos, E. Oset, Nucl. Phys. A **671** (2000) 481.

[38] M. D. Scadron, *Advanced Quantum Theory*, Third Edition, Imperial College Press, London (2007)

[39] B. A. Lippmann, J. Schwinger, Phys. Rev. **78** (1930) 469.

[40] `https://github.com/iarbina/meson_nuclear_states`

[41] Y. R. Kwon, F. Tabakin, Phys. Rev. C **18** (1978) 932.

[42] B. V. Numerov, Mon. Not. Roy. Astron. Soc., 84 592.

[43] A. Baca, C. García-Recio, J. Nieves, Nucl. Phys. A **673** (2000) 335.

[44] E. Oset, A. Ramos, Nucl. Phys. A **635** (1998) 99.

[45] W. Weise, Nucl. Phys. A **832** (2010) 51.

[46] D. Gazda, E. Friedman, A. Gal, J. Mareš, Phys. Rev. C **76** (2007) 055204; **77** (2008) 045206; **80** (2009) 035205.

[47] A. Ciepý, E. Friedman, A. Gal, J. Mareš, Phys. Rev. C **84** (2011) 0452006.

[48] A. Ciepý, E. Friedman, A. Gal, J. Mareš, Nucl. Phys. A **925** (2014) 126.

[49] J. Mareš, A. Cieplý, N. Barnea, E. Friedman, A. Gal, Proc. Sci. , 26th International Nuclear Physics Conference, (2016).

[50] A. Cieplý, J. Smejkal, Nucl. Phys. A **919** (2013) 46.

[51] A. M. Green, S. Wycech, Phys. Rev. C **71** (2005) 014001.

[52] T. Inoue, E. Oset, M. J. Vicente Vacas, Phys. Rev. C **65** (2002) 035204.

[53] N. Kaiser, P.B. Siegel, W. Weise, Phys. Lett. B **362** (1995) 23.

[54] M. Mai, P. C. Bruns, and U. G. Meißner, Phys. Rev. D **86** (2012) 094003.